UNIVERSIDADE FEDERAL DE MINAS GERAIS

DOCTORAL THESIS SUBMITTED TO THE GRADUATE PROGRAM IN ELECTRICAL ENGINEERING

A Practical Toolset for TERS Experiments and Analysis

Author:
Hudson Luiz Silva de MIRANDA

Advisor:
Prof. Dr. Ado Jorio de VASCONCELOS

A work submitted in fulfillment of the requirements for the degree of Doctor in Electrical Engineering

in the

Nanospectroscopy Laboratory
Graduate Program in Electrical Engineering

November 23, 2020

Universidade Federal de Minas Gerais

Escola de Engenharia

Programa de Pós-Graduação em Engenharia Elétrica

A PRACTICAL TOOLSET FOR TERS EXPERIMENTS AND ANALYSIS

Hudson Luiz Silva de Miranda

Tese de Doutorado submetida à Banca Examinadora designada pelo Colegiado do Programa de Pós-Graduação em Engenharia Elétrica da Escola de Engenharia da Universidade Federal de Minas Gerais, como requisito para obtenção do Título de Doutor em Engenharia Elétrica.

Orientador: Prof. Ado Jorio de Vasconcelos

Belo Horizonte - MG

Novembro de 2020

TESE DE DOUTORADO Nº 342

A PRACTICAL TOOLSET FOR TERS EXPERIMENTS AND ANALYSIS

Hudson Luiz Silva de Miranda

DATA DA DEFESA: 06/11/2020

Miranda, Hudson Luiz Silva de.
M672p A practical toolset for TERS experiments and analysis [recurso eletrônico] / Hudson Luiz Silva de Miranda. - 2020.
1 recurso online (xiii, 70 f. : il., color.) : pdf.

Orientador: Ado Jório de Vasconcelos.

Tese (doutorado) - Universidade Federal de Minas Gerais, Escola de Engenharia.

Apêndices: f. 61-63.
Bibliografia: f. 65-70.

Exigências do sistema: Adobe Acrobat Reader.

1. Engenharia elétrica - Teses. 2. Nanotecnologia - Teses. 3. Grafeno - Teses. 4. Raman, Espectroscopia de - Teses. I. Vasconcelos, Ado Jório de. II. Universidade Federal de Minas Gerais. Escola de Engenharia. IV. Título.

CDU: 621.3(043)

Ficha catalográfica: Biblioteca Prof. Mário Werneck, Escola de Engenharia da UFMG.

UNIVERSIDADE FEDERAL DE MINAS GERAIS
Escola de Engenharia
Programa de Pós-Graduação em Engenharia Elétrica

"A Practical Toolset for TERS Experiments and Analysis"

Hudson Luiz Silva de Miranda

Tese de Doutorado submetida à Banca Examinadora designada pelo Colegiado do Programa de Pós-Graduação em Engenharia Elétrica da Escola de Engenharia da Universidade Federal de Minas Gerais, como requisito para obtenção do grau de Doutor em Engenharia Elétrica.

Aprovada em 06 de novembro de 2020.

Por:

Prof. Dr. Ado Jorio de Vasconcelos
(UFMG) - Orientador

Confirmação por e-mail

Prof. Dr. Jaime Arturo Ramirez
DEE (UFMG)

Confirmação por e-mail

Prof. Dr. Davies William de Lima Monteiro
DEE (UFMG)

Confirmação por e-mail

Prof. Dr. Leandro Malard Moreira
DF (UFMG)

Confirmação por e-mail

Prof. Dr. Eduardo Bedê Barros
Fisica (UFC)

Confirmação por e-mail

Dr. Bráulio Soares Archanjo
Div. de Materiais (INMETRO)

UNIVERSIDADE FEDERAL DE MINAS GERAIS

Abstract

Escola de Engenharia
Graduate Program in Electrical Engineering

A Practical Toolset for TERS Experiments and Analysis

by Hudson Luiz Silva de MIRANDA

This work proposes a set of hardware and software tools to improve the usability of tip-enhanced Raman spectroscopy (TERS) systems. TERS is capable of providing optical images with resolution beyond the light's diffraction limit while also providing chemical and structural information, which makes it a technique of interest for nanoscience and nanotechnology applications. Specifically, this work aims to develop hardware and software solutions to better understand the TERS probe's interaction with an electromagnetic field, providing insights on: optical probe alignment methods, optimization of probe's constructive parameters and super-resolution.

Aside from the development of the necessary instruments, this task also comprehends the study of TERS probe's interaction with light via Finite Element Method simulations in addition to TERS experiments with graphene under a series of environmental conditions that affect the local electromagnetic field in a controlled manner.

Furthermore, the work also comprehends the use of data analysis techniques, specifically Spectral Unmixing and Principal Component Analysis (PCA), with the objective of efficiently extracting information from hyperspectral images in a non supervised manner via dimensionality reduction.

UNIVERSIDADE FEDERAL DE MINAS GERAIS

Resumo

Escola de Engenharia
Graduate Program in Electrical Engineering

Um conjunto de ferramentas prático para experimentos e análises TERS

por Hudson Luiz Silva de MIRANDA

Este trabalho propõe um conjunto de ferramentas de hardware e software para melhorar a usabilidade de sistemas de espectroscopia Raman aprimorada por ponta (TERS, do inglês *Tip Enhanced Raman Spectroscopy*). O TERS é capaz de fornecer imagens ópticas com resolução além do limite de difração da luz, além de fornecer informações químicas e estruturais, o que o torna uma técnica de interesse para aplicações em nanociência e nanotecnologia. Especificamente, este trabalho visa desenvolver soluções de hardware e software para melhor compreender a interação da sonda TERS com um campo eletromagnético, fornecendo informações sobre: métodos de alinhamento óptico de sonda, otimização dos parâmetros construtivos da sonda e super-resolução.

Além do desenvolvimento dos instrumentos necessários, esta tarefa também compreende o estudo da interação da sonda TERS com a luz via simulações do Método dos Elementos Finitos, além de experimentos de TERS com grafeno sob uma série de condições ambientais que afetam o campo eletromagnético local de forma controlada.

Além disso, o trabalho também compreende a utilização de técnicas de análise de dados, especificamente Decomposição Espectral (*Spectral Unmixing*) e Análise de Componentes Principais (PCA, do inglês *Principal Component Analysis*), com o objetivo de extrair informações de imagens hiperespectrais de forma eficiente e não supervisionada via redução de dimensionalidade.

Agradecimentos

Nada que vale a pena ser construído, é construído sozinho. Portanto é mais do que adequado reconhecer a contribuição de diversas pessoas nessa longa trajetória que me levou até o presente momento.

Primeiramente gostaria de agradecer profundamente aos meus pais, Sérgio e Geralda, por me oferecerem todos os meios e apoio para que eu pudesse trilhar meu caminho. Agradeço também aos meus irmão, Pedro e Flávio, que estão ao meu lado desde sempre. À minha namorada Bianca também extendo os agradecimentos por ter sido minha parceira e uma fonte de motivação e de humanidade.

Agradeço meu orientador e amigo Ado Jório por estar me guiando desde 2012 quando comecei minha iniciação científica. Seu apoio e confiança em minha capacidade foram fundamentais para trilhar minha trajetória profissional, desde o ciclo básico da graduação até hoje.

Agradeço ao Gusta e Thiago Vasconcelos, grandes amigos, cientistas e agora sócios que sempre não pouparam esforços para ajudar em minha formação.

Agradeço ao Cassiano, um companheiro constante e estupendo na nano-luta desde o mundo acadêmico ao empresarial, além dos preciosos conselhos de vida.

Agradeço também à equipe do LabNS que foi minha segunda casa por quase oito anos. Dentre eles: Andreij, Aroldo, Arthur, Catariana, Douglas, Emerson, Fabiano, Filomeno, Fred, João, Laura, Leandro, Lucas, Márcia, Plinio, Rafael Alencar, Raigna, Renan, Tiago e Vitor.

Agradeço ao Patryk Kusch, Stephanie Reich e colaboradores da FUB pelas contribuições valorosas e apoio ao trabalho realizado.

Agradeço ao Projeto NA@MO em seus realizadores, gestores e equipe técnica que me permitem trabalhar todos os dias com coisas que me trazem sentimento de realização.

Agradeço à UFMG, Escola de Engenharia, ICEx, DCC e PPGEE pelo ensino público, gratuido e de qualidade que me foi fundamental para meu desenvolvimento profissional e pessoal.

Contents

List of Symbols

λ	Wavelength	m
$\vec{E}$	Electric Field Intensity	V/m
$\vec{D}$	Electric Flux Intensity	C/m^2
$\vec{H}$	Magnetic Field Intensity	A/m
$\vec{B}$	Magnetic Flux Intensity	Wb/m^2
$\vec{J}$	Electric Current Density	A/m^2
ρ_v	Volume Charge Density	C/m^3
ϵ	Permittivity	F/m
μ	Permeability	H/m
NA	Numerical Apperture	$-$
F_{TERS}	Spectral Enhancement	$-$
D	Probe Apex Diamenter	nm
L	Nanopyramid Size	nm

"O que é verdadeiramente importante é a educação básica, para que a população esteja apta a se desenvolver, a aprender mais, a ter uma educação superior e a criar tecnologia, ela própria. A educação deve ter como objetivo dar uma base fundamental para uma vida melhor da população e ser capaz de criar conhecimento novo para um mundo novo que está diante de nós." - José Leite Lopes, CBPF, 1998.

Chapter 1

Introduction

Scientific advances are marked by the technological capacity to measure new phenomena. Two examples are the optical microscope, enabling the field of microbiology, and the spatial telescope, which allowed a much deeper study of celestial bodies. Despite the many advances, optical microscopy's resolution is physically limited by the light diffraction limit, known as Abbe's Limit [1]. This limit determines an approximate equation for the maximum spatial resolution of an optical measurement system:

$$d \approx \frac{\lambda}{2NA} \tag{1.1}$$

Equation (1.1) gives the smallest resolvable feature size d as a function of light's wavelength λ and the illumination collection's numerical aperture NA. When the separation between two emitters becomes smaller than d they become unresolvable from one another, as shown in Fig. 1.1.

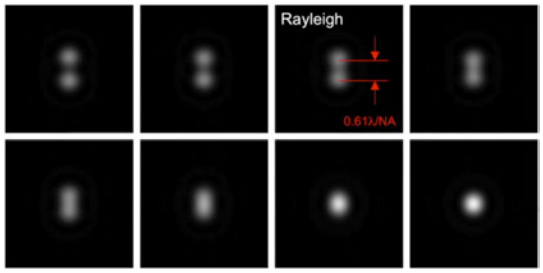

FIGURE 1.1: Images generated by two point light sources varying the space between them, providing a graphical representation of Abbe's Limit. When the two point-like sources are too close ($d < {}^{0.5\lambda}/_{NA}$), their PSFs superpose, precluding the identification of two distinct sources.[2]

From an image processing perspective, the performance of an optical system can be associated with a Point Spread Function (PSF), a 2-dimensional impulse response that represents the image acquisition setup. Usually, for microscopy setups, the PSF is an Airy disk [3] whose width depends on λ and NA, as shown in Fig. 1.2.

Given this limitation of optical images, it would not be possible to directly employ optical measurements at a nanometric scale, considering visible light has wavelengths in the range of 380 nm to 740 nm. There are two main aspects that motivate the need for nanoscale optical measurements. The first aspect is the wide range of possible applications of nanotechnology currently being prospected (Fig. 1.3). This creates a demand for study and quality control of nanomaterials involved in these applications, which gives rise to the second aspect: optical images are capable of

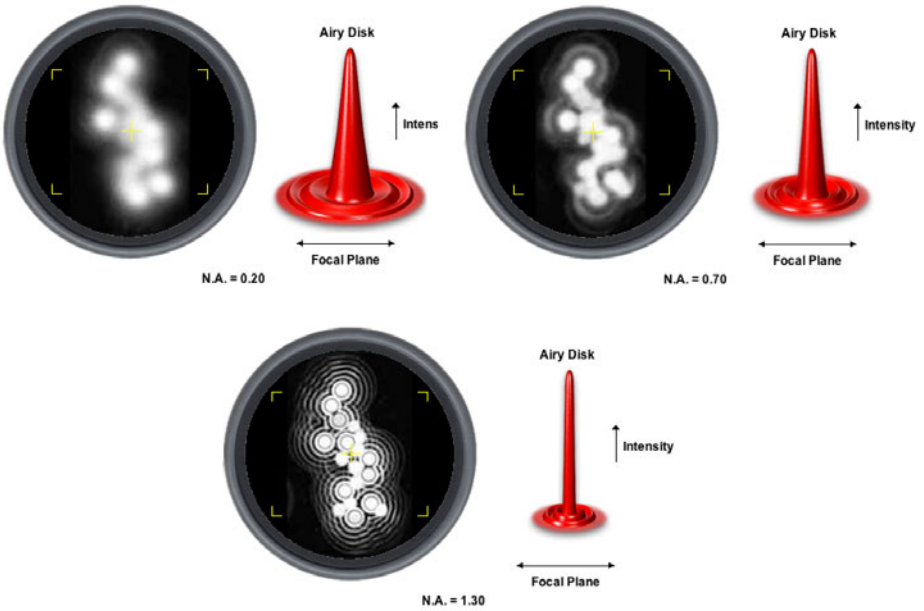

FIGURE 1.2: Simulation of formed images of point-like sources with Airy disks in systems with distinct NA. A higher NA results in a sharper Airy disk and improved spatial resolution, although always limited to the diffraction (Abbe) limit. The imaged point-like sources reveal the PSF of the system.[4]

providing a high level of information regarding composition, structure of materials and functional properties, more so than techniques such as Scanning Electron Microscopy, X-Ray Diffraction and Mass Spectroscopy [5].

The necessity of studying nanomaterials via optical means has encouraged the invention of modified microscopy setups for this task. Such devices include Stimulated Emission Depletion (STED) microscopes [5] and Tip Enhanced Raman Spectroscopy (TERS) [7]. The working principle of STED is based on fluorescence and TERS is based on Raman scattering, which makes it more sensitive to composition and structure and, for this reason, it will be the focus of this work. TERS combines Raman Spectroscopy [8], which provides a fingerprint of an analyte in the form of a Raman spectrum, and Scanning Probe Microscopy that provides topological information regarding the surface of the material [9]. The combination of a metallic scanning probe with a sharp apex, in association with a laser excitation source focused on it, generates an antenna effect concentrating the excitation power and amplifying the light scattered by the analyte, thus increasing the spatial resolution.

This work aims at supplying TERS users with a set of tools targeting crucial steps in performing the technique and also tools that provide a novel perspective when analysing experimental data obtaining TERS. Three main tools targeting these goals were produced during this work: on the experimental front, a reliable methodology for positioning a TERS tip optimizing optical signal and resolution is developed and tested; regarding the TERS probes, a simulation framework is elaborated to enable not only optimization of the probes' geometry and composition, but also to understand the distribution of electric field in a nanometric volume around the TERS probe apex; on the data analysis approach, the work proposes unsupervised algorithms that can assist in the exploration of large data sets of spectral data. With these tools some crucial issues in TERS probe design, probe alignment and TERS data analysis are tackled and demonstrated.

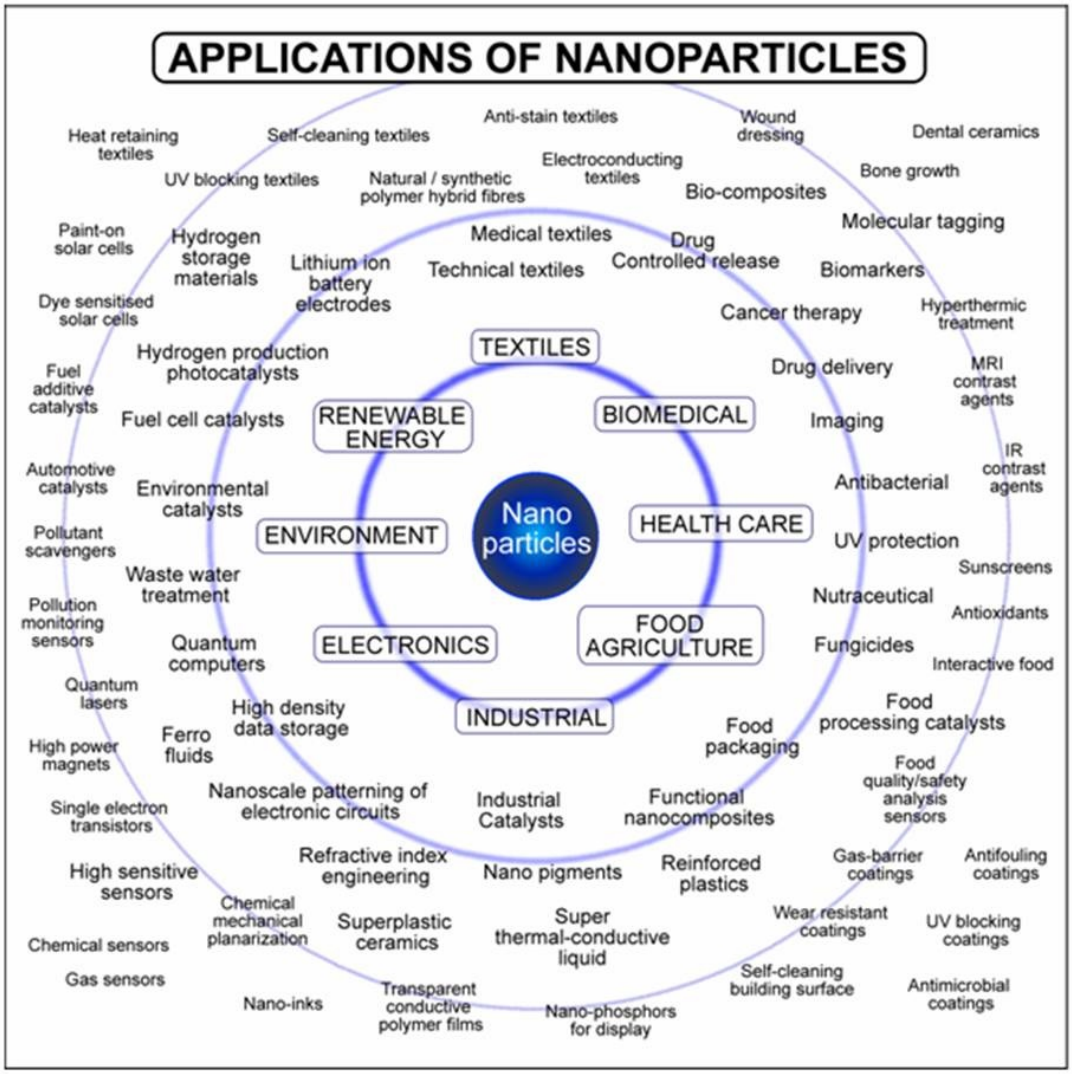

FIGURE 1.3: Range of possible applications of nanoparticles in different fields.[6]

The remainder of the thesis is structured in the following Chapters: Chapter 2 supplies the necessary background concepts that support this work. Chapter 3 describes the existing experimental apparatus and its required modifications for this work. The same chapter describes the simulation framework created to analyze TERS probes' response to optical excitation and also a set of algorithmic tools for large scale unsupervised Raman data analysis. Chapter 4 contains demonstrations and applications of the toolset presented in the previous Chapter. Finally, Chapter 5 summarizes the main findings produced by utilizing the developed toolset.

Chapter 2

Theoretical Background

This Chapter provides an overview of the relevant topics to understand the physical and engineering concepts required for this work.

2.1 Confocal Optical Microscopy

Optical Microscopy (OM) is a method for obtaining magnified images of small objects using visible light. Usually there is a light source that illuminates a sample and an objective lens collects the light after interacting with the sample and projects it onto an image sensor. The choice of how to illuminate the sample and how to collect the optical signal defines different types of OM. This work focuses on Backscattering Confocal Optical Microscopy (BCOM) [10, 11]. The basic diagram for this configuration is shown in Fig. 2.1. A collimated excitation light is transmitted through a beam splitter or dichroic mirror and it is focused by an objective lens onto the sample. The scattered light is then collected through the same lens and it is reflected by the mirror to another lens that focuses the light through a pinhole onto a detector.

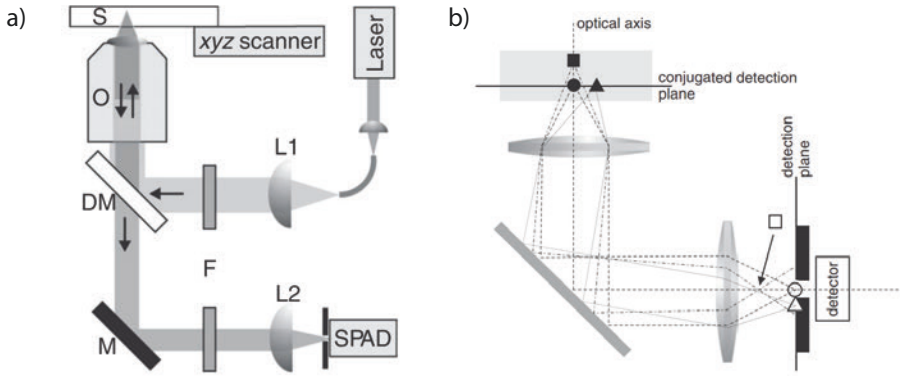

FIGURE 2.1: a) BCOM setup - the laser is directed to the sample by a dycroic mirror (DM) and through the objetictive lens (O); The light scattered by the sample (S) returns following the same path and it is transmitted by the DM, directed to a detector, in this case a Single Photon Avalanche Detector (SPAD); b) the pinhole in the way to the detector selects light scattered only in a small region around the focal point, acting as a spatial filter.[3]

In this setup, the pinhole in the front of the detector is responsible for the confocality. It acts as a spatial filter selecting light in a narrow region around the geometric

focal point. This results in a narrower PSF and focal plane [12], effectively improving the resolution. The optimal pinhole size, D_p, is defined by:

$$D_p \leq \frac{\lambda \cdot v_P \cdot M_T}{\pi \cdot NA}, \tag{2.1}$$

where λ is the collected wavelength, v_P is a parameter dependent on the system's PSF and is given in optical units, M_T is the total system magnification and NA the numerical aperture of the collecting lens.

The existence of the pinhole makes it necessary to scan a sample pixel by pixel (raster scanning) in order to obtain a full image, and this is a key limitation of BCOM.

Despite being optimized for spatial resolution, BCOM systems are still bounded by light's diffraction limit described by Eq. (1.1). Thus, classically, the resolution of the system can only be improved by decreasing the excitation wavelength λ or by increasing the numerical apperture NA.

2.2 Raman Spectroscopy

The Raman scattering effect refers to the inelastic scattering of light by matter [8]. This phenomenon consists in a change of an incident photon energy caused by their interaction with the scattering material. Therefore, if a material is optically excited with a given wavelength λ_{LASER}, the scattered light should present a small portion of light with different wavelengths. The amount of energy lost or gained depends on the sample's atomic vibrational structure, which, in turn, depends on its chemical composition, structure and environmental conditions [13]. The dependence between energy shift and material properties makes Raman a tool of great interest for materials characterization.

The amount of energy lost or gained by the photons (λ_{PHONON}) depends on the vibrational energy configuration of the material, as shown in Fig. 2.2.

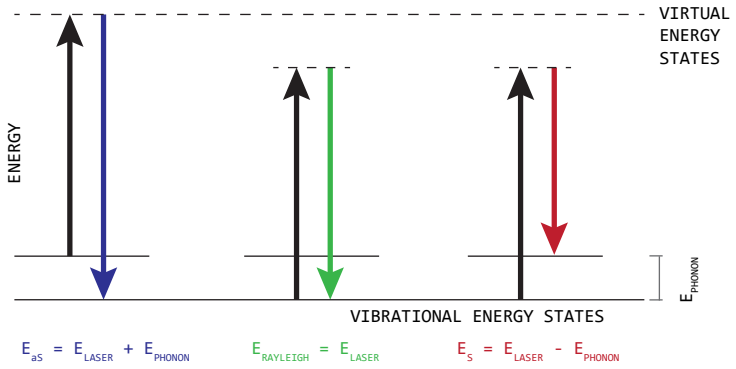

FIGURE 2.2: Band diagram for Raman scattering. In terms of scattered wavelength, the Stokes shift ($E_S = E_{LASER} - E_{PHONON}$) occurs towards higher wavelengths and the anti-Stokes ($E_S = E_{LASER} + E_{PHONON}$) goes in the opposite direction. The shift's magnitude (E_{PHONON}) is directly related to the phonon energy. The phonon is a quantum of atomic vibrational energy. (Source: Cassiano Rabelo)

Raman spectra are generally presented as graphs of Raman shift in units of wavenumbers (cm^{-1}) vs. signal intensity. Because the Raman shift occurs relative to the excitation wavelength, it is useful to perform a mathematical transformation

to present all spectra in the same reference, removing the excitation wavelength dependence from the visualization. This can be achieved by Eq. (2.2):

$$\Delta w = (\frac{10^7}{\lambda_{LASER}} - \frac{10^7}{\lambda_S}), \tag{2.2}$$

where λ_{LASER} and λ_S are the excitation and the scattered (Raman) wavelengths (in nm), respectively. Δw is the Raman shift (in cm^{-1}) and it is conventioned to be positive for Stokes and negative for anti-Stokes scattering.

Figure 2.3 illustrates the sensitivity of Raman spectroscopy to different graphene samples stacked in distinct amounts of layers. Only by analyzing the Raman spectral signature of a sample it is possible to determine the quantity of layers in a sample of graphene [14]. Figure 2.3 a) shows that graphene has two most prominent bands, named G and 2D. The G band is associated with the Carbon-Carbon bond stretching mode in an sp^2 hybridization configuration and the 2D band is generated by a breathing mode in the hexagonal rings [13].

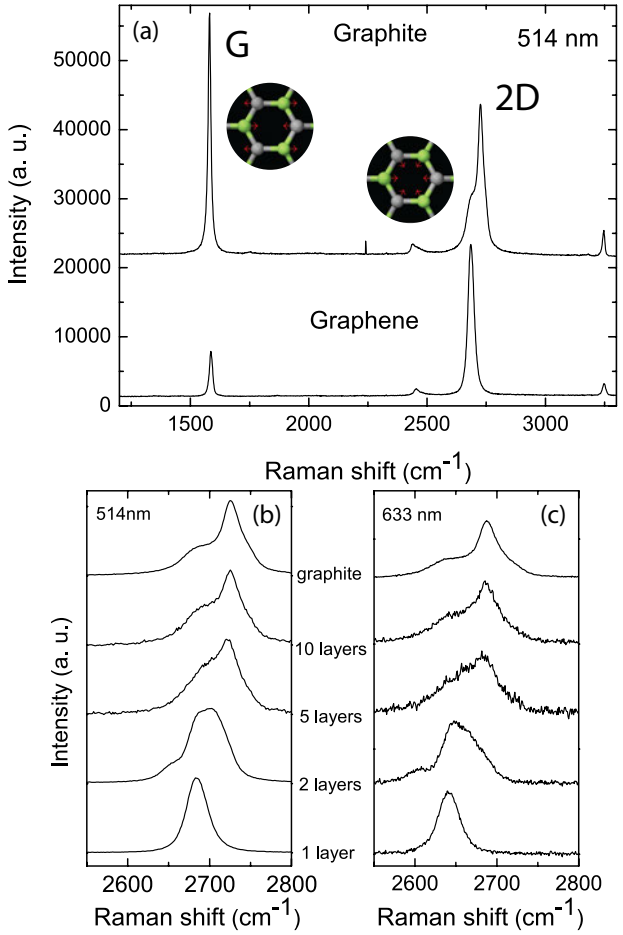

FIGURE 2.3: Raman Spectroscopy in graphene-related structures. a) shows the difference in Raman signature between single layer graphine and graphite, which is composed of a large number of stacked layers of graphene. The inset schematics depict the G and 2D vibration modes in the graphene structure [15]; b) shows the evolution of the 2D band shape as the number of layers increase, using a 514 nm excitation source; c) same as b), but with different excitation at 633 nm.(Adapted from [14])

The symmetry of the atomic structure, as well as the electric field distribution generated by the excitation light, will determine its Raman response. The Raman response of a material can be calculated from the Raman tensors, related to each of its vibrational modes, and input excitation electric field, given by the following formula:

$$\begin{bmatrix} E_{Sx} \\ E_{Sy} \\ E_{Sz} \end{bmatrix} = \begin{bmatrix} \alpha_{xx} & \alpha_{xy} & \alpha_{xz} \\ \alpha_{yx} & \alpha_{yy} & \alpha_{yz} \\ \alpha_{zx} & \alpha_{zy} & \alpha_{zz} \end{bmatrix} \cdot \begin{bmatrix} E_{Lx} \\ E_{Ly} \\ E_{Lz} \end{bmatrix}$$
$$\overrightarrow{E_S} = \overleftrightarrow{\alpha_R}\overrightarrow{E_L} \tag{2.3}$$

where the vector $\overrightarrow{E_S}$ represents the configuration of the scattered electric field, $\overleftrightarrow{\alpha_R}$ the Raman tensor for given vibrational mode and $\overrightarrow{E_L}$ the excitation electric field. It is important to consider that a molecule with N atoms will generally have $3N - 6$ degrees of freedom for atomic vibrations [13], each of them with an associated Raman tensor.

Being a two-dimensional material, the graphene response to an electric field excitation perpendicular to its plane generates no activation of the G band vibrational modes and negligible activation of the 2D band vibrational modes [16].

2.3 Scanning Probe Microscopy

Scanning Probe Microscopy (SPM) is a family of techniques consisting of scanning the surface of a sample with a small probe (or tip) and recording its physical properties [9]. These techniques resemble the operating principle of a vinyl disk player where the needle scans the surface and its deflection by patterns etched in the disk are transformed into sound.

From the wide range of SPM types, a technique denominated Atomic Force Microscopy (AFM), which provides information about the surface topography, will be the focus for this work. For this case a very sharp scanning probe with an apex in the range of few nanometers of radius is used. The probe follows the surface profile while a sensor monitors the magnitude of the interaction between the probe and the sample and feeds this value to a controller system that adjusts the probe height, usually via a piezoelectric actuator system, as depicted in Fig. 2.4. By scanning with this constant-gap configuration, it is possible to recover the sample topography by directly analyzing the voltage signal applied to the actuator system to maintain the constant gap. This voltage signal is usually converted to length units via a calibration constant.

The sharpness of a probe and the controller tuning are the main parameters to determine the quality of an AFM setup. If the controller is not correctly tuned it will not follow the sample's profile correctly and may also damage the probe during the scan. Furthermore, if the probe is too large, it will not be able to properly resolve features that are smaller than its apex diameter. This is exemplified in Fig. 2.5. In the case of SPM, the PSF is dependant on the shape of the probe and control system response, since the image is formed by physically convolving the probe with the surface [9].

Since the PSF for an SPM imaging system is defined by the shape of the nanometric probe, the resolution is much superior to optical images. The main limitation of SPM is the amount of information that can be extracted. AFM, for example, is

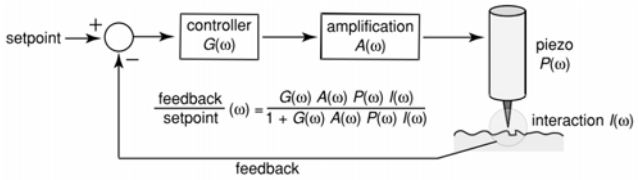

FIGURE 2.4: AFM control system diagram. A setpoint defining the desired value for the interaction is usually provided by an operator. During the operation, this value is compared to the current feedback signal and the error is sent to a controller. The controller's output is sent to a high voltage amplifying stage that drives a piezoelectric element that changes the probe's position along the Z axis while scanning the surface (XY plane) [3].

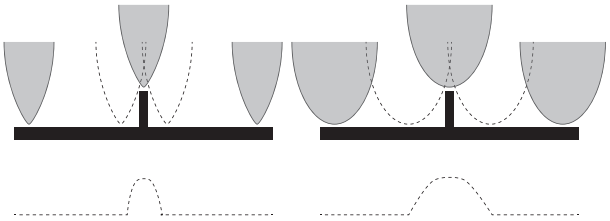

FIGURE 2.5: Schematics of an SPM procedure, where the tip (gray) scans a surface (black). A sharper probe generates a topographic image with better resolution, as displayed by the dashed line under the pictures.

only able to obtain topological and interaction (the one used for distance feedback) information [9].

AFM systems work based on the van der Walls force between the probe and the surface, and it can be categorized in three varieties: contact, non-contact and intermittent contact modes, according to the region of the van der Wall potential which is explored experimentally. In the contact mode, the probe is constantly engaging the sample and a sensor monitors the probe's interaction level caused by the contact and attempts to maintain a constant interaction defined by a setpoint value of a sensed variable (e.g.: deflection angle of a cantilever probe). The intermittent-contact mode, or tapping mode, is similar, differing in the fact that the probe oscillates vertically, reducing the amount of time the probe interacts with the sample. Non-contact mode consists in having the probe at a set distance from the sample throughout the whole scan. In this case, the feedback signal is related to the van der Waals force that arises from the small distance between the probe and the sample surface [17].

In order to sense the minute van der Waals forces, a specialized approach is necessary. Among different approaches, a well established solution, relevant to this work, is to use the scanning probe attached to a tuning fork (TF). The TF is forced to oscillate at its resonance frequency by a vibrating piezo element and, as the probe approaches the sample, the resonating frequency changes as a consequence of the interaction between probe and surface. A Phase Locked Loop (PLL) monitors change in phase and adjusts the piezo vibrating frequency in order to maintaing a constant phase [9]. The shift is compensated by moving the probe vertically to reestablish the working probe-sample distance and, consequently, the specified TF frequency shift. This provides the necessary tool to implement a control system that is able to maintain a reference distance between the probe and the scanned surface. The change in probe position along the vertical axis will then reflect the surface topography.

2.4 TENOM

Tip Enhanced Near-Field Optical Microscopy (TENOM) is a nanoscale optical imaging technique emerging from the combination of SPM and OM. The latter, as discussed in Chapter 1, is limited by the diffraction limit of light, which limits the spatial resolution of optical images to approximately $\lambda/2$. For light in the visible spectrum, this represents resolutions around a few hundreds of nanometers. Such limitation prevents the use of optical characterization in a critical range of applications, as shown in Fig. 1.3. The diffraction limited optical systems can be modified in order to obtain resolutions of the same order as SPM.

An approach to modifying optical systems to increase resolution beyond the diffraction limit is to position a metallic AFM probe in the focal region of a BCOM system, creating a TENOM system, as shown in Fig. 2.6.

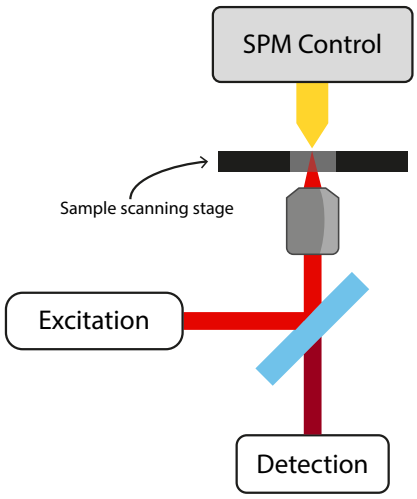

FIGURE 2.6: A TENOM system can be made by combininng BCOM and SPM with a metallic probe. The probe must be positioned at the BCOM system's focal spot with nanometric precision.[18]

As a usual BCOM system, a laser excitation source is present along with conditioning optics (can vary depending on the actual setup and experiment being performed) for the excitation and collected light that is directed to the detectors. A metallic scanning probe is then positioned at the optical system's focal spot with the assistance of an SPM system, acting as an optical nanoantenna. With proper positioning of the probe with respect to the optical system, the tip-laser alignment (axially and laterally), both SPM and BCOM systems will image the same region in a sample.

The presence of a sharp metallic tip made of a material compatible with the excitation wavelength produces an antenna effect [19]. This phenomenon contributes to the increased resolution via two distinct mechanisms: (1) the incoming light focused on the tip's apex induces plasmons in the metallic surface, which are amplified by resonance in the tip and then emit radiation [20]. This transforms the tip's apex in a nanometric light source illuminating the sample locally in the near-field optical regimen. (2) The light emitted by the probe excites the sample, generating scattered radiation. The scattered signal is composed of two components: the diffraction limited far-field (FF) and the highly localized near-field (NF) radiations [3]. The NF,

which decays exponentially with respect to the distance from the source, can only be detected up to a few nanometers away from the origin (in the case of visible light). Said probe utilized to locally excite the sample interacts with the NF component of the scattered light and, through the same plasmon resonance effect, amplifies it and converts it into a propagating wave, which can be detected with the same instruments as usual BCOM. These two phenomena result in both increased resolution and signal intensity.

2.4.1 TERS

TENOM is a technique that applies to several optical phenomena, like elastic (Rayleigh) scattering, photoluminecence, among others. When TENOM is combined with Raman spectroscopy, it gives rise to Tip Enhanced Raman Spectroscopy (TERS). The probe not only increases the spatial resolution, but it also significantly increases the signal-to-noise ratio in the Raman spectra. An enhanced Raman spectrum is shown in Fig. 2.7, as well as resolution improvements in optical Raman images.

A practical form of quantifying the TERS enhancement is to employ a metric denominated spectral enhancement, defined as:

$$F_{TERS} = \frac{A_{tip-down}}{A_{tip-up}}, \tag{2.4}$$

where F_{TERS} represents the spectral enhancement, $A_{tip-down}$ the integrated intensity of a Raman band in the presence of the TERS tip (composed of a sum of the far-field and the near-field regime) and A_{tip-up} the corresponding value in the absence of the tip (signal only from the far-field regime).

In addition to the spectral and resolution enhancements, because the probe is able to access the NF, the resulting Raman spectrum carries information that is normally not available through confocal Raman spectroscopy [21].

TERS has been vastly used to study carbon nanomaterias [24–28], biological materials [29, 30] and various other low-dimensional materials [7, 31]. The main hurdle of performing TERS, as with all TENOM applications, is the necessity to keep the probe stable in a small region around the geometric center of the focus spot, which is around tens of nanometers. The required mechanical, electrical, thermal and control stability to achieve this is one of the main challenges for TERS. This issue and possible solutions are discussed further in this work.

2.5 Simulations

In order to understand how the laser focus is formed and how it interacts with the probe, it is necessary to simulate electromagnetic waves and their behavior around metallic nanostructures. This can be achieved by applying a discretized and frequency domain version for Maxwell's Equations in a Finite Element Method (FEM) simulation [32]. Just as it is done for classical antennas, with the nanoantennas the focus of the simulations is to characterize signal amplification and electric field distribution in a steady state condition, thus the reason for using the frequency-domain

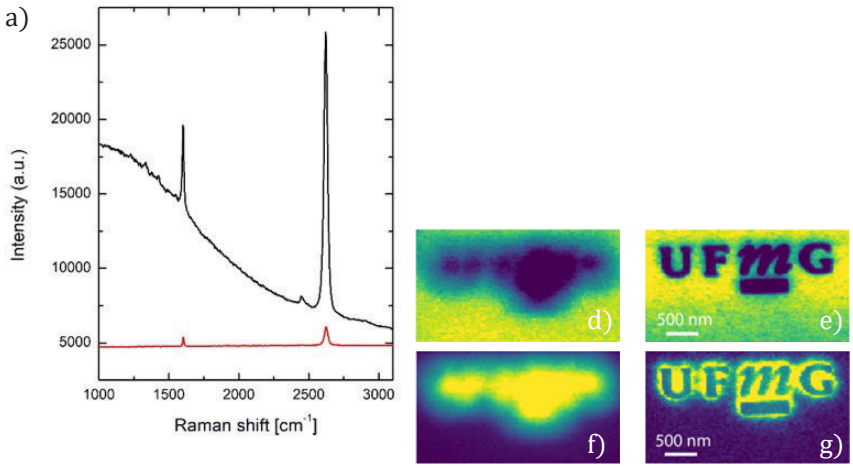

FIGURE 2.7: a) Graphene's Raman signature without the tip (red) and with the tip (black). The Raman peaks' amplitude is enhanced at the tip's location and a luminescence background is introduced by the tip (Adapted from [20]); b) $4 \times 4\ \mu m$ confocal Raman G band image of carbon nanotubes without tip; c) $4 \times 4\ \mu m$ G band TERS image of the same area as in (b), now the presence of a TERS probe [22]; d) confocal 2D Raman band image of a nano-scale graphene defect structure and e) image of the same region from d) using TERS; maps f) and g) are equivalent to maps d) and e) , but using the graphene's D band which associated with structural defect (panels d–g are courtesy of Inmetro produced with a method detailed in Ref. [23]).

FEM approach. In this work the frequency-domain differential form of Maxwell's Equations will be used [32]:

$$\begin{aligned} \nabla \cdot \vec{D} &= \rho_v \\ \nabla \cdot \vec{B} &= 0 \\ \nabla \times \vec{E} &= -j\omega\vec{B} \\ \nabla \times \vec{H} &= \vec{J} + j\omega\vec{D} \\ \nabla \cdot \vec{J} &= -j\omega\rho_v \end{aligned} \tag{2.5}$$

As well as the frequency-domain version of the constitutive relations:

$$\begin{aligned} \vec{D} &= [\epsilon]\vec{E} \\ \vec{B} &= [\mu]\vec{H} \end{aligned} \tag{2.6}$$

These equations are converted to a discrete form in order to be usable by FEM. Having the underlying physical equations that describe the optical phenomena that are of interest for this work, the FEM simulation requires other five components to be performed: a geometry representing the problem space must be provided; this is used by a meshing algorithm to produce the finite-sized elements for simulation; material properties, in this case the optical ones, must be attributed to each mesh element; boundary conditions should be specified to properly treat the limiting interfaces of the problem space; and, finally, an initial condition for the system must be provided (an optical excitation source, for example).

Having an input geometry that describes the problem space a meshing algorithm can be used to subdivide the ideal structure into finite-sized elements that are interconnected forming a mesh. These elements are usually tetrahedral because of its lower computational costs and ease of adaptation to various input geometries

(when compared to prismatic or hexahedral elements). The size of the meshing elements is crucial for the simulation's accuracy. The elements must be small enough to adapt correctly to the input geometry and also, in the case of optical simulations, they must be at least five times smaller (as a rule of thumb) than the smallest wavelength present in the simulation [32]. A good practice is to repeat the simulation varying the elements' size until the output variables converge. Naturally, there is a trade-off between discretization and computational costs: as the amount of elements increases, so does the amount of system memory used to represent this elements and the processing time for the simulation.

With the discretized structure, material properties must be assigned to each finite element. Specifically, for optical simulations, the complex index of refraction is sufficient to populate the medium parameters in the constitutive relations from 2.6. The index of refraction can be obtained form both theoretical models or experiments [33].

The boundary conditions of the simulation space are critical for optical simulations[34] because, without proper treatment, they act as perfect reflecting surfaces confining the wave inside the simulation space. Most FEM softwares, such as Comsol Multiphysics used in this work, provide options of boundary conditions to properly handle the simulation limits. These conditions can emulate, for example, a very good absorbing material and their formulation may depend on the type of wave being simulated (e.g.: plane wave, cylindrical wave, gaussian beam, etc.). An effective approach is to use a Perfectly Matched Layer (PML)[35] that is basically an anisotropic absorbing medium placed around the simulation space, this emulates an infinite medium around the specified geometry [32]. Boundary conditions can also be used to represent a symmetry of the simulation space, this can be useful to reduce it if the underlying problem being simulated presents mirror symmetries. For example, a perfect magnetic conductor (PMC) boundary condition imposes symmetry of electric fields and currents, thus it can be used as a symmetry constraint for optical simulations.

2.6 Data Processing and Analysis Techniques

Optical images offer a wide variety of results in different formats [36]. The first type of data are the conventional microscopy images representing a magnified object. Nevertheless, more complex data types can also be obtained, especially when using spectroscopy. A light spectrum is the decomposition of a light signal as a function of energy, which is usually expressed in electron-Volts [eV], wavelength [nm], frequency [THz] or wavenumber [cm^{-1}]. Figures 2.2, 2.3 and 2.7a), present such spectra, relating a particular wavelength or Raman shift to a signal intensity. Optical spectra can embody a significant amount of information [36]. In Raman spectroscopy (presented in Section 2.2), for example, each peak is related to a particular vibrational mode in the sample under analysis, which can be used to deduce composition and structure [14, 37, 38]. These data types open a wide field of data processing and analysis techniques ranging from simple signal processing, such as averaging filter, to classifiers that are able to identify a substance given its spectral signature.

In addition to single spectrum data, some equipments are capable of forming images where each pixel contains a complete spectrum, and this is called hyperspectral imaging (HSI) [39]. These are three-dimensional matrices where the first two dimensions are spatial location (x and y), corresponding to the region comprehended by the image, and the third dimension is spectral, comprehending the acquired spectral

range. An example of hyperspectral image is shown on Fig. 2.8. The combination of hyperspectral imaging and Raman spectroscopy was made possible by recent equipment advancements and is a frontier field of application, specially for TERS [21, 40, 41], as discussed in Section 2.4.1. This data format will be the focus of this work.

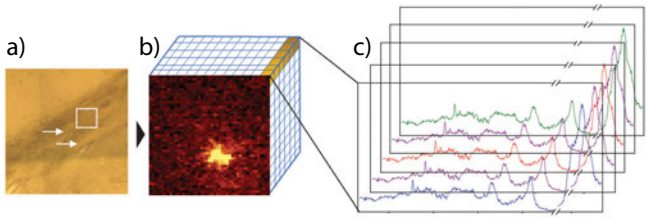

FIGURE 2.8: a) Microscopy image of a mice brain section; b) Synthetic image generated by performing a hyperspectral Raman scan in the region delimited by the white rectangle in a). The colors in b) are obtained by performing a feature extraction process for each pixel in the HSI, reducing each spectrum to a single value, which can be the intensity of one specific spectral feature; c) Illustrates how the depth of each HSI pixel contains a whole optical spectrum. (Adapted from [42])

In face of its high dimensionality and complexity, the visualization and analysis of HSIs is non-trivial. The most direct form to visualize a hiperspectral image is to reduce each spectrum to a single value based on a given metric. An usual metric for Raman spectroscopy is peak amplitude, as shown in Fig. 2.9. An estimate of peak amplitude can be achieved by simply detrending the data on a given range, this avoids the necessity of linear regression for peak parameter estimation, resulting in a simple HSI inspection method. However, this technique is very limited in its capacity to extract non-trivial information which may be contained in the data. Many characteristics in the sample can only be inferred through spectroscopy by analyzing a whole spectrum. An example of this can be seen on Fig. 2.3 where the amount of layers not only has an impact in all present peaks, but also changes the shape of the peak around 2700 cm^{-1}, the 2D band.

Given this complexity, HSIs can benefit from more elaborate data science tools, specially unsupervised learning techniques, as usually the data is unlabeled. This work will focus on two particular tools: Principal Component Analysis (PCA) and Spectral Unmixing. Both are essentially dimensionality reduction tools that require no input other than the data itself and the desired number of dimensions of the new dataset.

2.6.1 Principal Component Analysis

PCA is a well established tool for unsupervised data dimensionality reduction and feature extraction [43](a). It consists of applying linear transformations in the data, such as translations and rotations, in order to obtain a new feature space where the new axes are aligned with the directions of most variances, as depicted in Fig. 2.10. After the transformation, the new features are ordered with respect to explained variance. With this operation, the first component, PC_1, will contain the most variance and PC_N, where N is the number of dimensions in the original dataset, will be the least meaningful component in terms of variance. Another interesting aspect of PCA is that all the new components are perpendicular to each other, meaning that they are linearly independent.

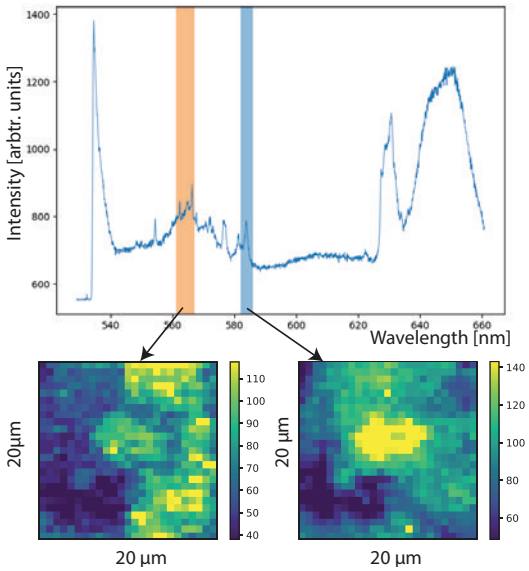

FIGURE 2.9: HSI visualization can be achieved by applying metrics along specific spectral ranges. In the image above, the metric applied is peak amplitude estimate within two different ranges. The data refers to Raman spectroscopy HSI of a mouse's brain slice. Particularly, when the metric is applied in the blue range, a bright region, corresponding to a β-amyloid plaque is revealed in the center of the image. This same plaque is barely visible under the orange range (Data source: Emerson Fonseca, unpublished).

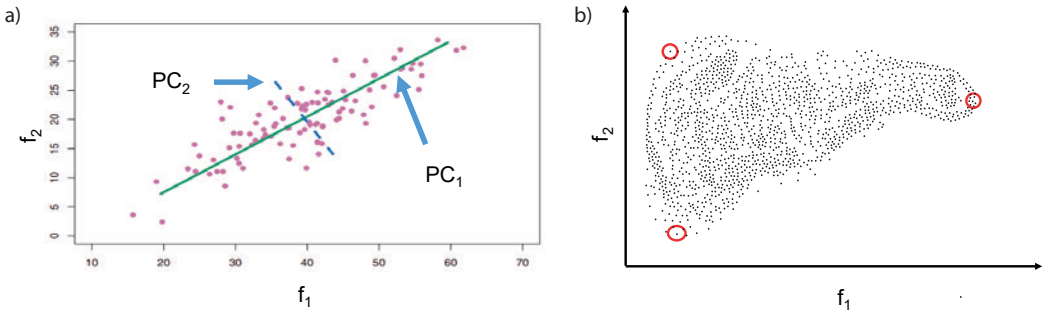

FIGURE 2.10: a) By rotating and translating the coordinate system, it is possible to obtain a new space where the principal components (PCs) are aligned with the directions of most variance successively (Adapted from [43]); b) In contrast, unmixing utilizes endmembers as components of a new feature space that represents each sample as a weighted average of the endmembers.

This technique is particularly interesting for spectroscopy, as spectral data usually contain a large amount of features, considering that each point in a spectrum is a feature. A particular study of Raman spectroscopy of graphene has shown that its possible to reduce the feature space from 1024 to three dimensions and maintain the necessary variance to explain the relevant dynamics in the data [36].

2.6.2 Spectral Unmixing

Similar to PCA, spectral unmixing can be used to reduce a feature space and streamline the investigation of HSIs. It consists of representing a dataset in terms of the

weighted average of extreme points, endmembers, in the data, as shown in Fig. 2.10(b). By selecting data points forming a convex hull (envelope) containing the dataset, it is possible to represent each data point inside this volume as a mixture of the hull's vertexes.

The unmixing process constitutes of two main steps: selecting the optimal endmembers from the dataset, then represent the entire dataset in terms of weighted averages of these endmembers. The process of extracting the endmembers can be done automatically by algorithms such as N-FINDR [44]. This algorithm selects endmembers maximizing the volume of the convex envelope, the simplex, formed by them. This is based on the assumption that the purest pixels in the dataset will yeld the largest volume for the corresponding simplex.

With the endmembers selected, they can be used to decompose the dataset. This can be done through several algorithms and the choice will depend on the underlying problem. In the case of Raman spectra, signature mixtures are additive when no change in vibrational modes arises from mixing two or more compounds. With this physical characteristic, methods that allow destructive combinations of endmembers are not desired. Under this condition, methods such Fully Constrained Least Squares (FCLS)[45] can be used obtain the optimal combination of the endmembers to represent a given spectrum in the dataset.

Considering this the whole processing pipeline is unsupervised, spectral unmixing serves as a powerful tool for HSI exploration [46]. It is also possible to validate the performance of the unmixing operation by performing the inverse operation: using the calculated endmembers and weights to reconstruct the spectra and quantify their difference from real data by using methods such as Root Mean Square Error (RMSE) or Pearson Correlation Coefficient(PCC).

Spectral unmixing differs from PCA in terms of interpretation as the new space is represented in terms of existing data, supplying a direct interpretation, and PCA generates a representation in terms of the PC's, which may not have a direct interpretation.

Chapter 3

Methods

3.1 TERS System

The TERS system implemented is a combination of BCOM with non-contact AFM. This choice is optimized for a high NA excitation and collection, but it limits the setup to the analysis of transparent thin samples, as the excitation light must be transmitted through the sample in order to interact with the tip and then be collected through the inverse path.

3.1.1 Optical Path

Figure 3.1 displays the system's optical path. In sequential order from laser to detectors the elements are:

1. Laser - He-Ne laser with 632.8 nm wavelength and 21 mW power output (Model HNL210L, Thorlabs);

2. Laser Line Filter - Narrow band-pass filter to clean-up the laser output spectrum (Model LL01-633-12.5, Semrock);

3. Beam Expander - Pair of lenses with 30 mm and 250 mm focal distances to expand the beam diameter by a factor of 8.3× in order to match the objective lens entrance diameter. (Model AC254-030-A, AC254-250-A, Thorlabs);

4. Radial Polarizer - Changes a linear polarization to radial, which, when tightly focused, generates a strong component along the propagation direction [47]. The resulting field will have the same orientation as the probe (vertical) resulting in optimal optical coupling (Model RPC, ARCoptix);

5. Spatial Filter - Removes undesired components generated by the radial polarizer. Consists of a focusing lens (f=40 mm), a pinhole (D=10 µm) and a collimating lens (f = 45 mm). The pinhole must be positioned along the optical axis and near the focal position in order to block undesired non-radially polarized components generated by the previous element (Model AC254-040-A-ML, P10D, AC254-045-A-ML, Thorlabs);

6. Berek Compensator - A variable waveplate [48] used compensate phase shifts produced by optical elements between the radial polarizer and the sample that would destroy the radial polarization (Model 5540M, Newport Inst.);

7. Microscope - A standard inverted microscope to accommodated the sample, objective lens, scanning table and video cameras (Nikon Plan Apochromat VC 60x Objective 1.4 NA, MCL Nano-H50, Model Eclipse Ti-U, Nikon);

After the microscope, the scattered signal can be directed to two outputs: a) Photon Counter and b) Spectrometer:

8. Pinhole (Output: a, b) - Provides the system's confocality, as discussed in Figure 2.1 (Models P100D(a) and P150D(b), Thorlabs);

9. Collimation Lens (Output: a, b) - As the laser beam exits the microscope, it is focused in an exterior point. This is done by manufacturer in order to place optical sensors in this position, but since it would not be viable to put the available detectors so close to the microscope, the beam is recollimated (Model AC254-200-B-ML(a), AC254-150-B-ML(b), Thorlabs);

10. Notch Filter (Output: a, b) - Filters out the Rayleigh component from the laser beam (Model LP02-633RU-25(a, b), Semrock);

11. Focusing Lens (Output: a) - Focuses the laser on the photon counter's sensor (Model AC254-100-B-ML, Thorlabs);

11. Focusing Lens (Output: b) - Focuses the laser on the spectrometer's input slit. The lens' NA should match the spectrometer's specification (Model AC254-30-B-ML, Thorlabs);

12. Bandpass filters (Output: a) - Set of optical filters to select a specific wavelength range. As most photon counters can not distinguish wavelengths, it is necessary to perform this step to guarantee that only the desired wavelength range is being detected;

13. Photon Counter (Output: a) - An avalanche photodiode (APD) responsible for photon counting (Model SPCM-AQRH-14, Excelitas);

14. Spectrometer (Output: b) - The combination of a spectrometer and a CCD camera capable of acquiring optical spectra with high sensitivity (Model SR-303i, DU401A-BR-DD, Andor).

The system employs both a photon counter and a spectrometer coupled to a Charge Coupled Device (CCD) because these devices have complementary specifications. The photon counter, in this case an avalanche photodiode (APD), is capable of counting individual photos and can be used to generate Raman maps with very low exposure times per each pixel (< 100 ms per pixel). Its only drawback is that it is not able to distinguish between different wavelengths, thus optical bandpass filters must be placed on its aperture to select only the wavelength range that is relevant for a given experiment. In contrast, the spectrometer, coupled with a CCD, is capable of separating and measuring different wavelengths, generating actual optical spectral graphs as outputs, the only drawback being exposure time which must usually be in the order of a couple of seconds in order to obtain results with acceptable signal-to-noise ratio.

3.1.2 AFM system

The AFM setup is a home-made system based on a R9 SPM Controller form RHK Technologies. The system is able to perform non-contact AFM utilizing tuning forks (TF) with a 32.8 kHz resonance frequency and a PLL system to control the probe-sample distance. In this setup, the controller has three main functions: controlling

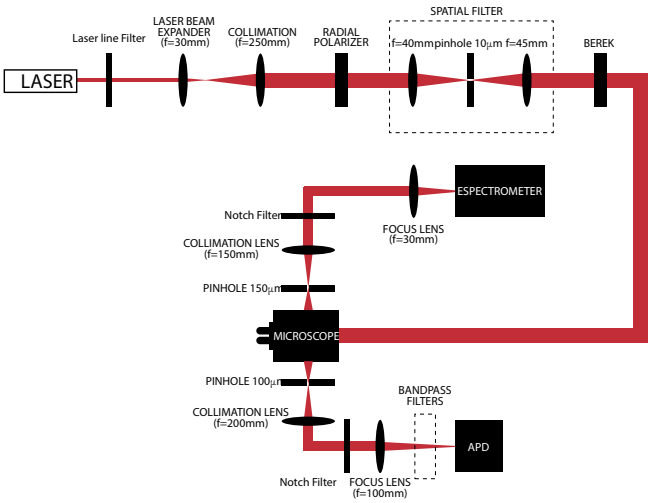

FIGURE 3.1: The TERS optical system. The excitation generated by the laser undergoes a conditioning process for radial polarization and directed to a microscope where the sample is located. The output beam can be directed to either a spectrometer equiped with a CCD or an APD for optical detection.

the scanning probe's distance to the sample, control the sample's XY movement stage for scanning and synchronizing detectors with the scanning procedure.

In order to operate, the probe, which is attached to the TF, must be connected to a positioning system with nanometric precision in three axes. In addition, this system must handle the TF's excitation at the resonance frequency and the detection of the oscillation signal for control purposes. The structure that handles these functions is denominated scanhead and is depicted on Figure 3.2. On the optical setup, the scanhead is placed on top of the inverted microscope (Item 7 in the optical path) in such way that the probe protruding from the bottom face of the scanhead can reach the sample's surface.

As shown in Figure 3.2 a), the scanhead is supported at three points of contact consisting of fine thread screws. One of the screws, with an attached red box, is a linear actuator based on a picomotor (Model 8302, Newport) capable of moving with a sub-micron precision and locking into a given position. This element is used to bring the scanhead close enough to the sample's surface in order to be in range for the Z piezo actuator, which has a total range of approximately 1.5 µm.

In the central part of the scanhead a metal tube containing cylindrical piezo elements is located. These piezo actuators are responsible for aligning the probe's apex with the laser focus along the XY plane and also maintaining the constant gap between the probe and the sample's surface. These elements are controller by the R9 Controller via high voltage DC signals.

3.2 Probes

Considering that the TERS setup is based on a He-Ne laser with a 632.8 nm wavelength, a probe manufactured with compatible materials and shape must be used. A gold pyramidal tip denominated Plasmon-Tunnable Tip Pyramid (PTTP) manufactured in partnership with Dimat/Inmetro was used [20, 49]. Their geometry is composed by a pyramid on top of a truncated pyramid, as shown in Figure 3.3. This

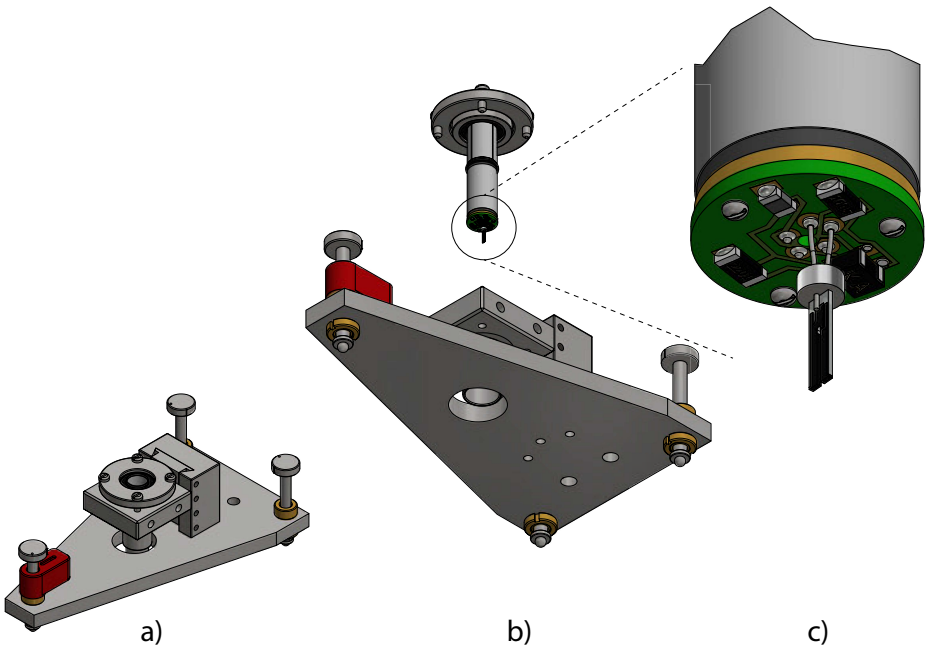

FIGURE 3.2: a) Shows a top view of the scanhead's mechanical structure (electronics omitted for better visibility); b) Bottom view with detail of the piezo tubes responsible for the nanometric XYZ positioning inside the scanhead; c) Detail of the tunning fork soldered to a signal amplifying stage for oscillation measurement.(Source: Vitor P. Monken)

particular shape and subwavelength size creates a Localized Surface Plasmon Resonance (LSPR) effect [20, 50], which that improves the signal enhancement capabilities of the probe. The choice of gold is based on its chemical stability, its plasmonic activity and low absorption for He-Ne laser excitation at 632.8 nm.

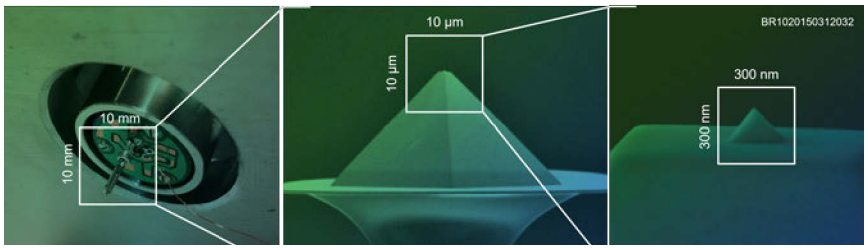

FIGURE 3.3: Detail of the PTTP probes used in this work. The figure on the left shows a photo of the TF soldered in the amplifying circuit, as schematically show in Fig. 3.2(c). The middle and right pictures show details of the probe, which consists of a gold nanopyramid on top of a truncated micropyramid, forming a resonant cavity for the surface plasmon polaritons(Adapted from [20]).

3.3 Probe Scanning System (PSS)

In the experimental setup, images are obtained by raster scanning the sample along the XY plane by means of the sample positioning stage, while the tip is fixed at the laser focus position. Nevertheless, in order to study the light-probe coupling within

the laser focus, scanning a region in the XY plane by moving the probe and having the laser and sample in a static position is necessary. Such system was developed in the scope of this work by creating a separate control hardware for the XY piezos located in the scanhead along with the associated software to implement the scan logic and acquisition of optical data.

3.3.1 PSS Hardware

The additional and preexisting hardware for this task is shown on Figure 3.4. It consists of a Digital-to-Analogic Converter (DAC), specifically a NI9263 and a custom high voltage amplifier (courtesy of Prof. Roberto Paniago-DF/UFMG). In this setup, the NI9263 receives data from the software via USB connection and generates an analog signal in a ± 2.5 V range with a resolution of 0.3 mV for X position and Y position separately and are transmitted through coaxial cables with BNC terminations. These signals then serve as inputs for the voltage amplifier which has a gain of roughly $38\times$, resulting in a range of ± 95 V and a 11.5 mV resolution. The amplifier has symmetric outputs for each channel: X+, X-, Y+ and Y-, as required by the piezo system.

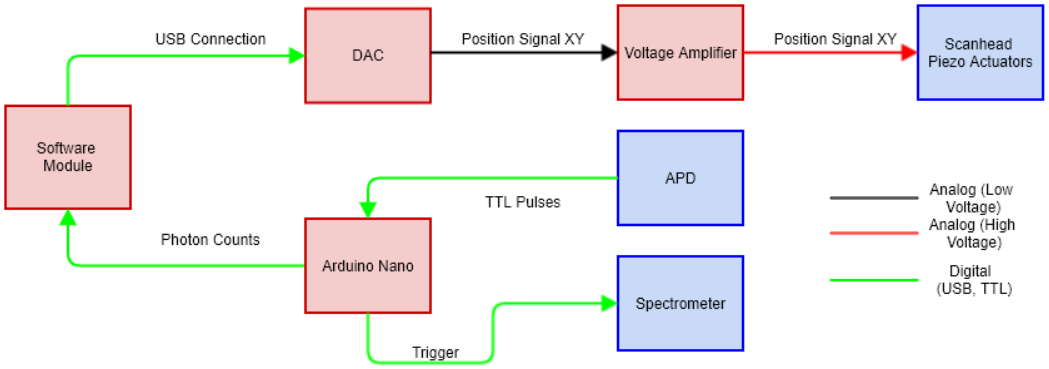

FIGURE 3.4: PSS hardware diagram. The blue boxes are existing modules in the TENOM system and the red ones were added modules to create the PSS functionality. The types of the signals exchanged by the boxes is outlined in the image.

The hardware must be calibrated before usage in order to obtain the proper conversion factor from volts to nanometers. The calibration procedure consists of a topographic scan of a well know AFM reference pattern, as shown in Figure 3.5. In this case the R9 Controller is used in place of the NI9263 to drive the amplifier, as the PSS software does not have access to topographic data.

The PSS must also be able to generate optical images with an APD. The APD used in the system is a SPCM-AQR-14 (Perkin Elmer), which generates a TTL pulse each time it registers a photon in its detector, therefore an increase/decrease in light input intensity will result in a increase in photon counts per unit of time. To count the APD TTL pulses an Arduino Nano was used in association with the Arduino Frequency Counter Library [51]. The micro-controller simply counts the TTL pulses received within a given integration time and writes the resulting counts/second (Hz) value to the USB port, which is then read by the PSS.

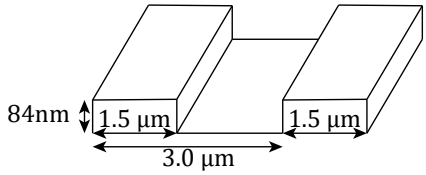

FIGURE 3.5: Schematics of an AFM standard with the reference sample dimensions. The square wave pattern is repeated throughout a 2×2 mm^2 area.

3.3.2 PSS Software

The hardware requires a software to generate position commands to the DAC for scanning and read photon counts from the APD's Arduino to form an image. For this purpose a software was developed in C++ using the Qt Toolkit along with National Instrument's Application Programming Interface (API) to send commands to the NI9263. This software was registered at the Instituto Nacional de Propriedade Industrial under the name Probe Master (BR512020001027-0).

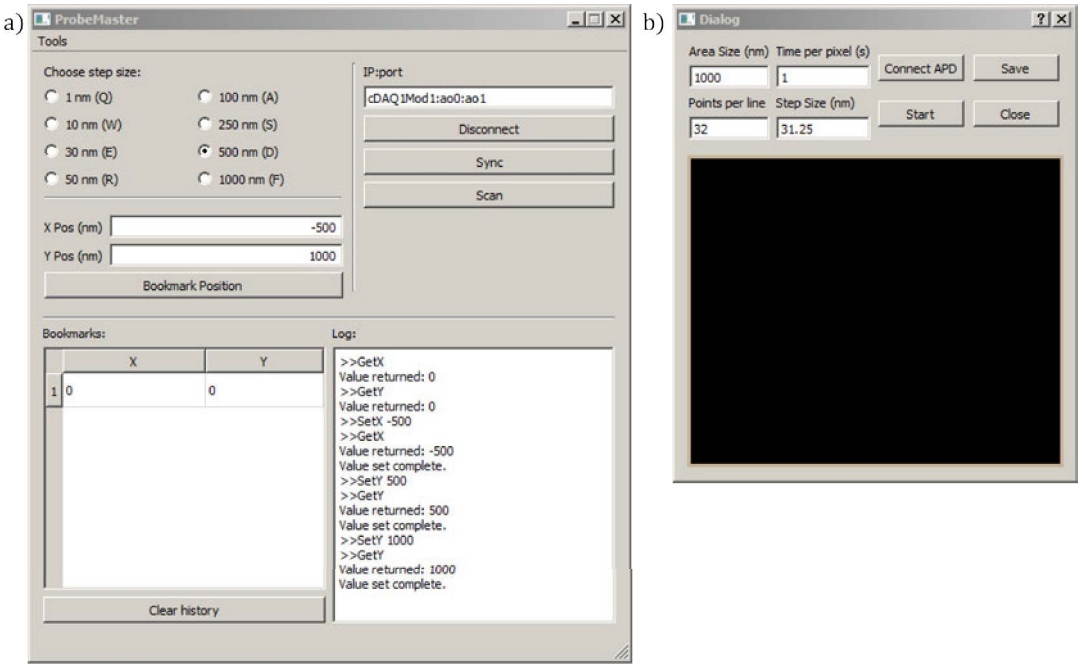

FIGURE 3.6: a) PSS's main window for manual tip control and logging; b) Scan window providing scan parameters and an image preview updating in real time.

The software's main screen is shown in Figure 3.6 a). It provides a Connect and Disconnect button and an address dialog to establish a connection with the DAC. It provides a range of fixed step sizes and enables the user to move the probe via the keys I, K, J, and L for Up, Down, Left and Right steps. The X Pos and Y Pos text displays show the current position already converted from Volts to nanometers, which can be bookmarked to be reused. All the actions are shown in a logger for debugging purposes.

The scan window shown in Figure 3.6 b) supplies buttons to connect to the APD's Arduino, start/stop scanning, save data in binary format (.dat) and close window button. It also provides text displays to enable adjustment of scanning parameters,

namely the scan area size (only square images are currently supported), integration time per pixel, number of points to acquire for each line and the step size between each pixel. The images are produced around the probe's current position. Additionally it provides a real time display of the image being generated.

3.4 Nanomanipulation System (NMS)

Another possible approach for interacting with the laser and sample is by manipulating the probe with an haptic device. This concept has already been used for cantilever-based SPM systems [52]. Nanomanipulation is useful to intuitively interact with the nanometric world in a controlled manner. It can be used, for example, to study strain in nanometric structures such as carbon nanotubes [24].

A nanomanipulation system (NMS) consisting of an haptic device, shown in Figure 3.7, capable of controlling the probe in the XY plane and converting optical intensity, as measured by the APD, into mechanical resistance in the haptic device's arm is proposed. In this scenario, the user manipulates the device's pen to change the voltage signals applied to the scanhead's piezo tubes while providing a force feedback that is dependent on the APD's signal.

FIGURE 3.7: Geomatic Touch Phantom haptic device used in the nanomanipulation application. The arm is able to register pose in 3D space with 6 degrees of freedom (DOF) and generating forces on the end effector (pen's point) with 3 DOF (X, Y and Z).

The central idea of this system is to use the optical signal intensity to intuitively align the probe in the position that corresponds to a maximum intensity. Alternatively, for other applications, the feedback signal can be mapped to the TF's frequency shift signal, which is dependent on the Wan der Walls force sensed by the probe, giving a measure of the amount of interaction between probe and sample, creating a framework for nanomanipulation. The feedback signal is then translated to a mechanical resistance or force in the haptic arm to give the user an intuitive feeling of the magnitude of these physical variables.

3.4.1 NMS Hardware

The NMS was in implemented as a part of this work and was built on top of the current system described previously. Figure 3.8 shows the added components. The new system takes control of the probe's XY movement and is able to monitor a range of different signals to use as haptic feedback.

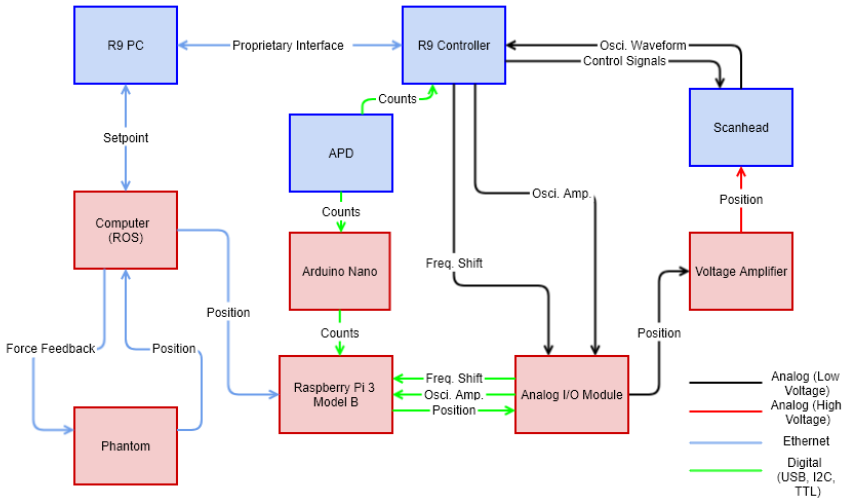

FIGURE 3.8: NMS hardware architecture. The blue boxes correspond to elements already present in the TERS system. The red boxes represent components introduced for the NMS. The connection types are indicated in the legend.

For the probe movement, the Phantom device sends its current position to a computer that processes it and relays to a Raspberry Pi 3 Model B. This device converts the position signal received via USB to I2C signal that is transmitted to two MCP4725 12-Bit DACs located in the Analog I/O module, one for X and another for Y positions. These DACs' output are within a $[0, 5]$V range that is converted to a $[-2.5, 2.5]$V by an offset circuit shown in Figure 3.9, for compatibility with the high voltage amplifier (same device used for the PSS).

In this setup, the high voltage amplifier and Arduino Nano are the same as in the PSS. In contrast, the APD counts are first relayed to the Raspberry, only then to reach the PC in order to compute the feedback force.

3.4.2 NMS Software

The NMS Software architecture is built on top of the Robot Operating System (ROS) framework [53]. It provides a structure that encapsulates executable modules into nodes that exchange messages and can seamlessly operate in a distributed environment.

The solution is divided into three nodes, one running on a PC with Ubuntu 16.04 LTS operating system (OS) and another two running on a Raspberry Pi 3 Model B with a Rasbian 9.3 OS (Figure 3.10). The PC runs the *phantom_node*, written in C++, and it is responsible for communicating with the haptic device via OpenHaptics Toolkit[54] in order to read position data and write force feedback data for the haptic device to apply. This node is also responsible for managing the dynamically changeable parameters in the application via a standard user interface supplied by

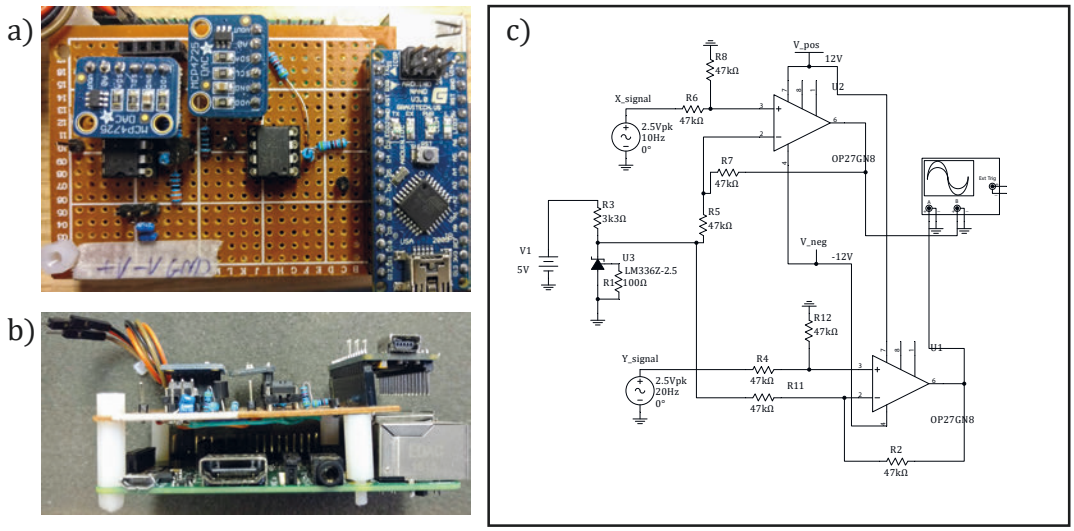

FIGURE 3.9: a) and b) show top and side views of the Analog I/O Module, Raspberry and Arduino. c) shows the diagram for the voltage range conversion. These components are enclosed on a metal box and are powered by a PC power supply.

ROS. In addition, the *phantom_node* processes the raw position data and, for safety, only allows the device's position to act on the actual probe if a button on the device's pen is pressed. Furthermore, all movement will be considered with respect to the probe position from the moment this button was pressed. This allows a "click and drag" usage to move the probe, increasing the manipulation precision while maintaining range. This is further refined by having a sensitivity parameter that controls how much a pen movement will affect the probe's actual position. Equation 3.1 is responsible for implementing this behavior:

$$R^2_{k+1} = R^2_k + \alpha(R^1_{device} - R^1_{click}), \tag{3.1}$$

where the 2 superscripts indicate positions in the probe coordinate system and the 1 subscripts position in the haptic device coordinate system. R^2_{k+1} is the new probe position being calculated, R^2_k is the present position, α is the sensitivity parameter, R^1_{device} is the current device position and R^1_{click} is the device's position at the moment activation button was pressed.

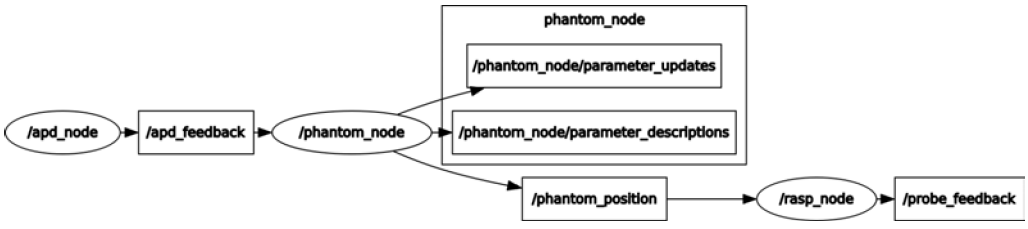

FIGURE 3.10: Graph of the components in ROS. *phantom_node* runs on a Ubuntu PC and incorporates the haptic feedback device and the dynamic parameters servers. *rasp_node* is responsible for the interaction with analog IO devices and *apd_node* communications with the APD's Arduino to provide a continuous stream of optical feedback measures, both nodes run on the Raspberry device.

Another main task of the *phantom_node* is to calculate the feedback force based

on the optical feedback amplitude. Firstly, the feedback value is normalized within a range set by the user. In sequence, it can be converted to a normalized feedback force by one of four rules:

$$\begin{array}{lcll} F & = & Ax & \text{Linear} \\ F & = & x^A & \text{Exponential} \\ F & = & \frac{e^A}{e^A-1}(1-e^{-Ax}) & \text{Inverted Exponential} \\ F & = & -x^A+1 & \text{Negative Exponential} \end{array} \tag{3.2}$$

These force mappings could be selected by an user in order to not only favor sensitivity to lower or higher feedback signal but also invert the trend of the mapping. The impact of these force mapping strategies is further discussed in Section 4.2.4.

3.5 Analysis Software

In order to analyze HSIs generated by the equipment, a GUI based software was developed. This program, written in Python V 3.6, supports tools for data exploration, conditioning and it also implements spectral unmixing with the assistance of a library called PySptools [55] for spectral data analysis. This program was written by Cassiano Rabelo, Eduardo Ribeiro, Jailton Coelho, João Luiz E. Campos, Taiguara Tupinambás and myself.

The software implements a full workflow for HSI exploration and analysis. The process starts with file support for binary files, Witec format text files and the widely used Flexible Image Transport System (FITS) format with the assistance of the *pyfits* library. After loading an HSI, the user is presented with the UI depicted in Fig. 3.11. In this context, it is possible to explore the spectra contained in the imported file and select wavelength ranges (shown in color over the spectrum) in order to form band intensity maps, as shown in the additional windows in Fig. 3.11.

The main window also provides the user with the functionality of spike removal, as will be detailed in Section 3.5.1 and filtering. For the bandpass filter functionality, the user can adjust the cutoff frequencies in normalized units. The goal of this filtering process that acts on each spectrum separately as a time series is to remove frequencies lower and higher than the ones that for the actual Raman peaks, reducing the impact of spectral background and acquisition noise in further analyses. This process is essentially a feature extraction process to be optionally used prior to the spectral unmixing.

The spectral unmixing algorithm implements the steps described in Section 2.6.2 using N-FINDR [44] and FCLS [45] implementations from PySptools. For this process, the software enables the user to choose the amount of endmembers and the spectral region to run the algorithm.

After performing the spectral unmixing operation, the results are shown in a new context such as in Fig. 3.12. This new window shows the endmembers that were chosen by the N-FINDR algorithm and maps of the contribution (weights) of each endmember to the overall HSI. These maps are denominated abundance maps, as they represent the how much of each endmember contributed to the real signature of each spectrum. Additionally, this interface also provides an error map to quantify the reconstruction error using the RMSE and PCC metrics.

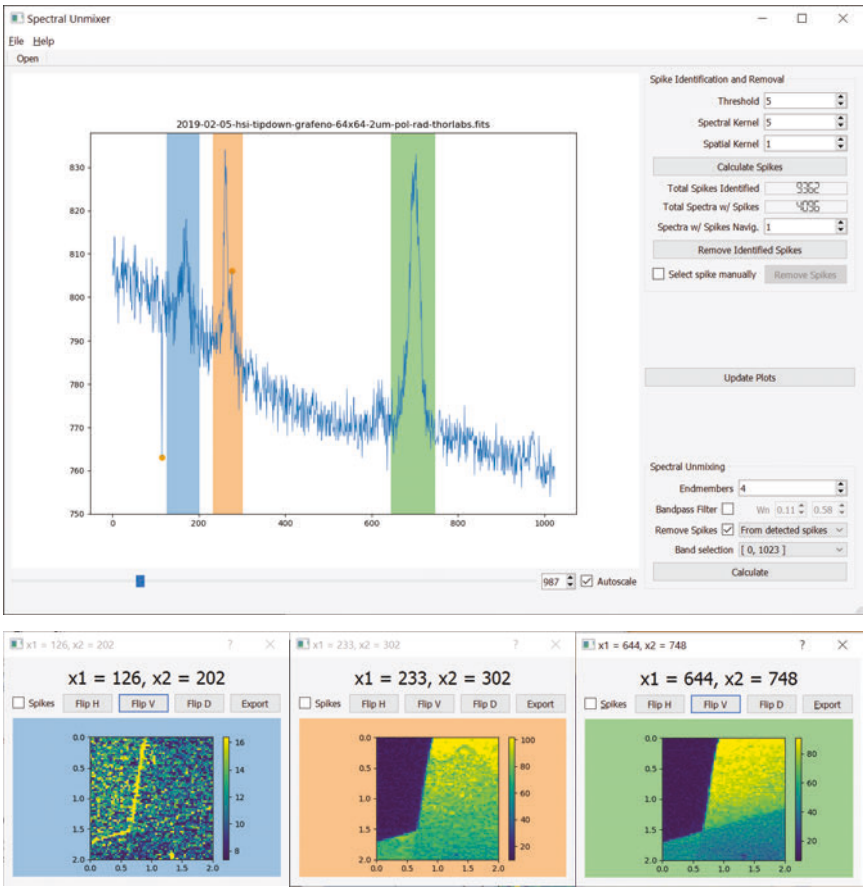

FIGURE 3.11: Main interface for the Spectral Unmixer software for HSI exploration and unmixing. The main window provides tools for spectrum exploration, intensity map generation, outlier removal, filtering and spectral unmixing. The secondary windows shown in the bottom portion display various intensity maps extracted from the corresponding selected bands, as matches by color codes.

3.5.1 Spike Removal Tool

Outliers in spectral data can be caused by charged particles that randomly go through the spectrometer's optical sensing area during a data acquisition. These outliers can be detrimental to the performance of both spectral unmixing and PCA algorithms as they will contaminate endmembers and PCs. Figure 3.13 shows an example of two cosmic rays affecting a graphene spectrum.

In order to remove these outliers, one can take advantage of their significant amplitude difference and the fact that they are highly unlikely to appear in the same spectral region of spacially neighboring pixels. Given these aspects, the following algorithm is proposed to remove cosmic rays while preserving the amplitude of actual Raman peaks.

Step 1. Perform a three-dimensional median filter in the HSI;

Step 2. Get the filtered signal by subtracting the original HSI from the filtered one;

Step 3. Calculate the standard deviation of the resulting HSI from the previous step;

Step 4. Compare each value in the HSI obtained in Step 2 to a threshold composed of the standard deviation multiplied by a constant adjustment coefficient;

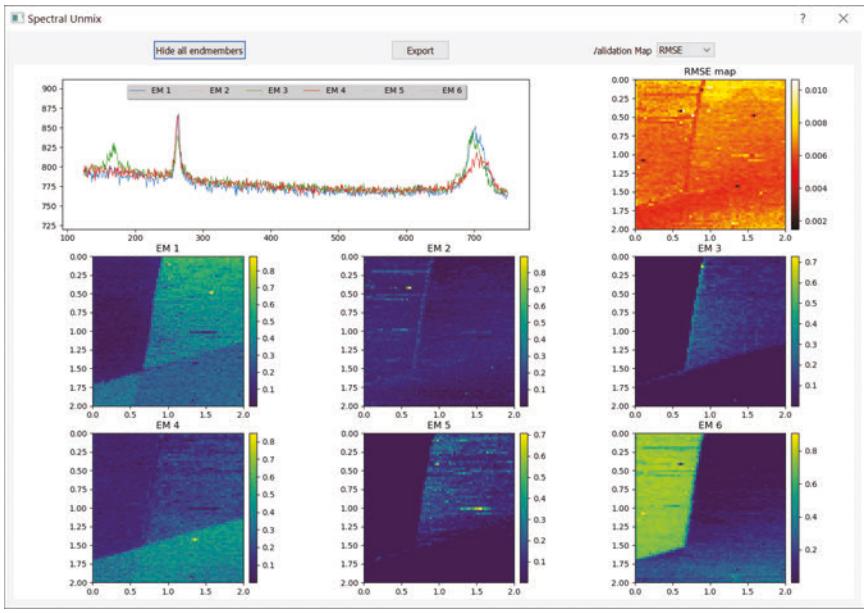

FIGURE 3.12: Unmixing result context window showing the endmemberds in the upper left corner, the abundance maps in the botton portion and the error map in the upper right corner. This windows also enables exporting the result as text data and PDF.

Step 5. For each value that exceeds the threshold, replace the value in the original HSI by the median of its neighbors (both spectral and spatial).

With this procedure, only regions in a spectrum that are flagged as outliers will be effectively modified. Another benefit of this algorithm is the fact that it takes into consideration the information of neighboring spectra, via the 3D median filter, making the procedure robust to cosmic rays of any spectral width.

3.6 Simulations

To obtain a better understanding of the behavior of the electric field in the focal spot, with the presence of a metallic tip, simulation methods can be employed. For this purpose the Finite Element Method (FEM) will be used, as it provides the necessary flexibility to simulate excitation source, tip and a sample.

3.6.1 Simulation Environment

The goal for the simulations is to analyze how different configurations of the TERS tip, laser excitation and sample substrate interact with each other forming the steady state electric field distribution that will excite the sample. For this purpose, the simulation environment must embody the Equation set 2.5 and 2.6. Comsol Mutiphysics V 5.3a was used, as it provides a package for Frequency Domain Wave Electromagnetic (FDWE) simulations on a FEM formulation that supports the underlying physics of interest.

The simulation space considered is a cylindrical region 3.8 µm wide and 4.2 µm high with the probe and substrate centralized in its inside. Figure 3.14 displays the disposition of these elements. The substrate is covered by a thin film region that can be composed of gold or glass depending on the desired experiment.

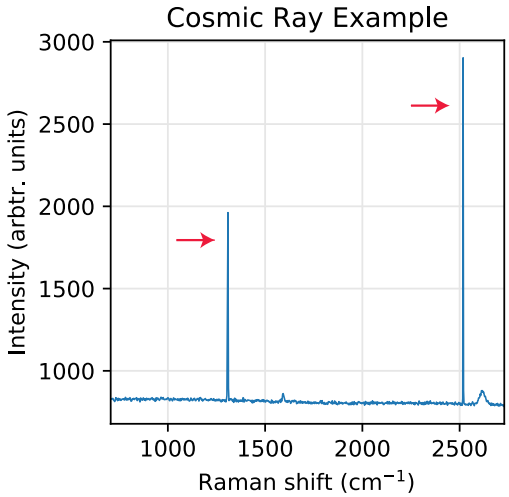

FIGURE 3.13: Example of two cosmic rays (indicated by red arrows) appearing in a graphene spectrum. This effect changes drastically the intensity measure for a range of one up to four pixels, usually.

The height of the pyramid, angles between faces and plateau length (upper face of micropyramid body) correspond to their actual dimensions from scanning electron microscopy images, as shown in Fig. 3.14. The probe's apex is modeled as a fillet to the nanopyramid's edges with a diameter D and said edges' length is denoted by L.

3.6.2 Boundary Conditions

The proposed environment has two kinds of symmetry that can be explored in order to specify boundary conditions that significantly reduce computational costs. The first symmetry is the cylindrical one for the enclosing space in the simulation. This enables the Comsol software to optimize the formulation of the 600 nm thick PML that surrounds the simulation environment. The probe and substrate geometries also present mirror symmetry with respect to the XZ and YZ planes, and this enables the insertion of PMC boundary conditions at these planes, in order to be able to only simulate a quarter of the problem space, improving computational costs and memory usage drastically.

3.6.3 Meshing

The geometry's mesh was defined using tetrahedral elements of second order, with an exception of the PML, which used prismatic and hexahedral elements. The tetrahedral elements adapt satisfactorily even to the probe's apex, as seen in Fig. 3.15 and the other element types enable the insertion of more elements across the PML's thickness, a key detail that improves its absorbance.

The shape of the elements and their regularity have significant impact in the simulation accuracy. A commonly used metric is the equiangular skew defined by:

$$S = 1 - max\left(\frac{\theta_{max} - \theta_e}{180 - \theta_e}, \frac{\theta_e - \theta_{min}}{\theta_e}\right), \tag{3.3}$$

where θ_{max}, θ_{min} and θ_e are the maximum, minimum and ideal equiangular angle for an element of a given type. This metric is closer to one as an element shape

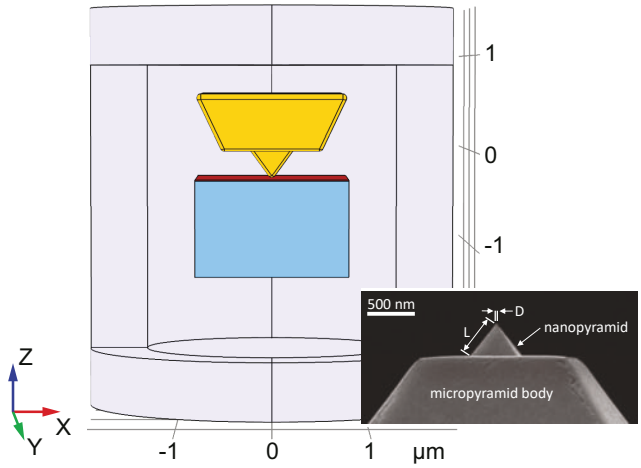

FIGURE 3.14: Geometry of the simulation space. The simulation comprises of three components: the PTTP gold probe shown in yellow; the substrate subdivided into blue region composed of glass and 12 nm thick region to simulate thin films; the regions indicated with light blue color represent the 600 nm absorbing layers that enclose the simulation space. The bottom right portion of the image shows a scanning electron microscopy (SEM) image of the PTTP probe utilized as reference for the simulation geometry (adapted from [56, 57]).

TABLE 3.1: List of mesh properties.

Parameter	Value
Mesh Vertices	252,545
Tetrahedra	1,167,806
Prisms	62,560
Hexahedra	20,000
Triangles	82,694

Parameter	Value
Quads	8,320
Edge elements	3846
Vertex elements	54
Avg. element quality	0.67
Min. element quality	0.11

approaches the shape of a regular element of the same shape. Regularity is crucial, as FEM assumes the distance between vertices of an element are equal. Figure 3.15 shows the distribution of this metric in the simulation space, with emphasis on the probe's apex region, which is the region of most interest for the simulations.

The table below also brings some relevant statistics for the mesh in this standard configuration ($D = 40$nm and $L = 450$nm):

As it can be see from Table 3.1 and Fig. 3.15, the problem space is extensive, but with adequate mesh element sizes (when compared to the excitation wavelength) and quality (as it can be see from the average and minimum element qualities).

Despite the complexity of the mesh, the basic simulation converges in approximately five minutes and three iterations on a machine equiped with an Intel i7-8700K processor and 32 GB of RAM running at 2,666 MHz.

3.6.4 Initial Conditions

Frequency domain simulations require an initial condition for the field distribution. In this case, the initial distribution is the laser excitation distribution in free space. The radially polarized, tightly focused Gaussian beam was approximated using the paraxial approximation for a Gaussian Beam with 360 nm waist diameter and polarization along the vertical axis (direction of propagation). Since the excitation is

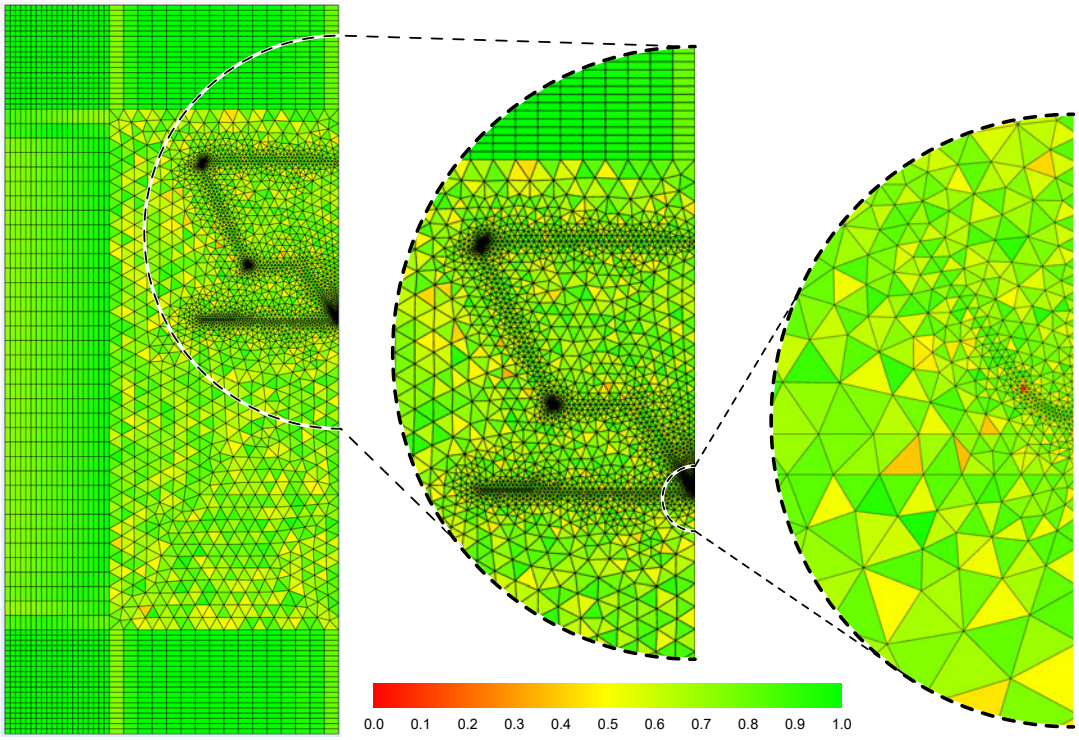

FIGURE 3.15: Meshing of quarter of the simulation space as determined by the PMC boundaries. The insets detail the meshing around the probe's apex. The color code represents element quality as determined by the equiangular skew metric. A quality of 1 (green) corresponds to an element with ideal shape and a quality of 0 (red) corresponds to a degenerate element.

purely along the vertical Z axis, only this component of a focused Gaussian beam must be taken into account when specifying the beam waist at the focal plane. Simulations for an excitation wavelength of 632.8 nm and 1.4 numerical aperture, as determined by our experimental apparatus described in Section 3.1.1, show that the value of the beam waist under these conditions is 360 nm [3].

Figure 3.16 shows the intensity distribution for the input excitation's $|E_z|^2$. The excitation is focused exactly on the surface of the sample and the maximum amplitude of the field was derived from a measurement of the total power reaching the sample in the experimental setup.

3.6.5 Materials

It is necessary to introduce the optical properties of the probe's material in the simulation software. The required input parameters are the real (n) and imaginary (k) parts of the refraction index. Those were obtained experimentally from reflection and transmission measurements of thin gold films by Johnson and Christy [33]. Both n and k are defined as a function of the wavelength in order to obtain a more accurate simulation environment.

The region surrounding the probe is composed of air with $n = 1$ and $k = 0$, unless a specific substrate is introduced. This approach, however, has a fundamental

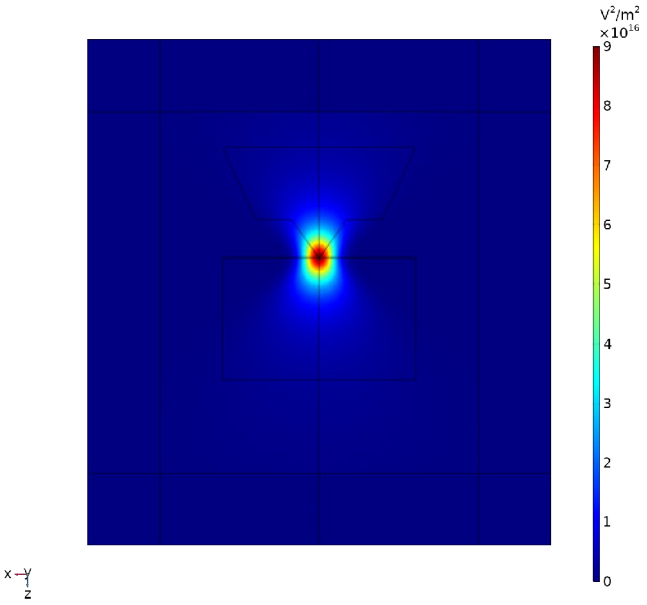

FIGURE 3.16: Intensity map for $|E_z|^2$ component of a Gaussian beam generated by paraxial approximation with 180 nm waist radius and polarization along the Z axis. The simulation space was mirrored with respect to the ZY plane with post-processing.

drawback. Nanometric conductive structures present a significantly spatially nonlocal dielectric function [58]. This phenomenon impacts the optical properties and renders them dependent on the size of the metallic structures. This dependency of optical constants on structural dimensions disallow the possibility of performing studies that involve comparison of results with varying excitation wavelength, therefore all simulations are performed with the fixed wavelength of 632.8 nm, matching the experimental setup.

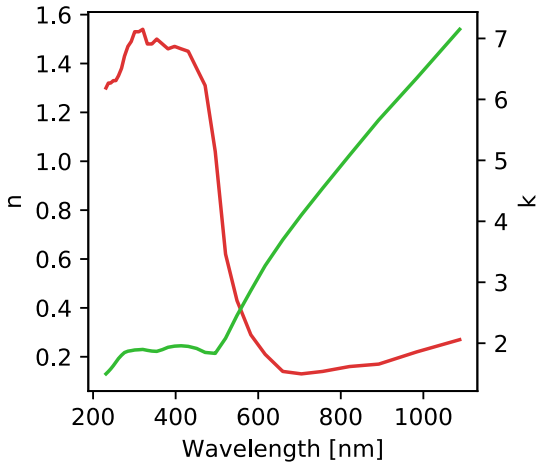

FIGURE 3.17: Real (n, red) and imaginary (k, green) portions of the refractive index for gold thin films. [33]

Chapter 4

Results

The present Chapter focuses on validating and application of the set of tools presented in the previous chapter, ranging from the simulations, hardware and software tools.

4.1 Simulations

This section covers simulation concerning the electric field distribution around focal spot and probe. Additional simulations are performed throughout Chapter 4 in the context of understanding the experimental results.

4.1.1 Electric Field Mapping in Free Space

The first step for using the simulation apparatus consists of determining the tip response to an electric field as described in Section 3.6.4. For this simulation, the probe parameters corresponding to the size of the nanopyramid (L) and the diameter of the tip apex (D) are set to 425 nm and 40 nm, respectively, as they represent an average probe with the current manufacturing process [20]. The $|E|^2$ is used for displaying the results, as TERS signals have a dependency with $|E|^2$ [59]. Figure 4.1 shows the simulation output for this set of conditions. The color map shown in a) represents the squared norm of the electric field scattered by the tip. It is possible to observe a high field intensity around the tip's apex. Furthermore, the field distribution close to the tip's body is consistent with theoretical calculations (see inset to Fig. 4.1a)) predicting that the nanopyramid acts as a resonance cavity for the surface plasmons [20].

To inspect the efficiency of the PML surrounding the simulation environment, Fig. 4.1b) depicts the logarithm of the distribution shown in a). It is possible to see that the intensity of $|E|^2$ is approximately seven orders of magnitude lower on the simulation bounds than on the tip's apex. Such attenuation levels demonstrate the efficiency of the designed PML layer. Interestingly, the same log distribution shows a degree of penetration of the eletric field into the metallic domain of the tip, which is expect for a non-ideal metal.

In addition, the field distribution along the sample plane (Fig. 4.1c)) shows the probe capacity of concentrating the electric field in a region smaller than the diffraction limit (the peak's FWHM is 30 nm). Another relevant characteristic of the field distribution is its predominant vertical (Z) polarization accompanied by a minimum of the horizontal component (X) in the central position. These distribution profiles are of significant importance in Raman spectroscopy, since they represent the excitation field and the direction of the electric field excitation that have direct impact in the measured Raman signal.

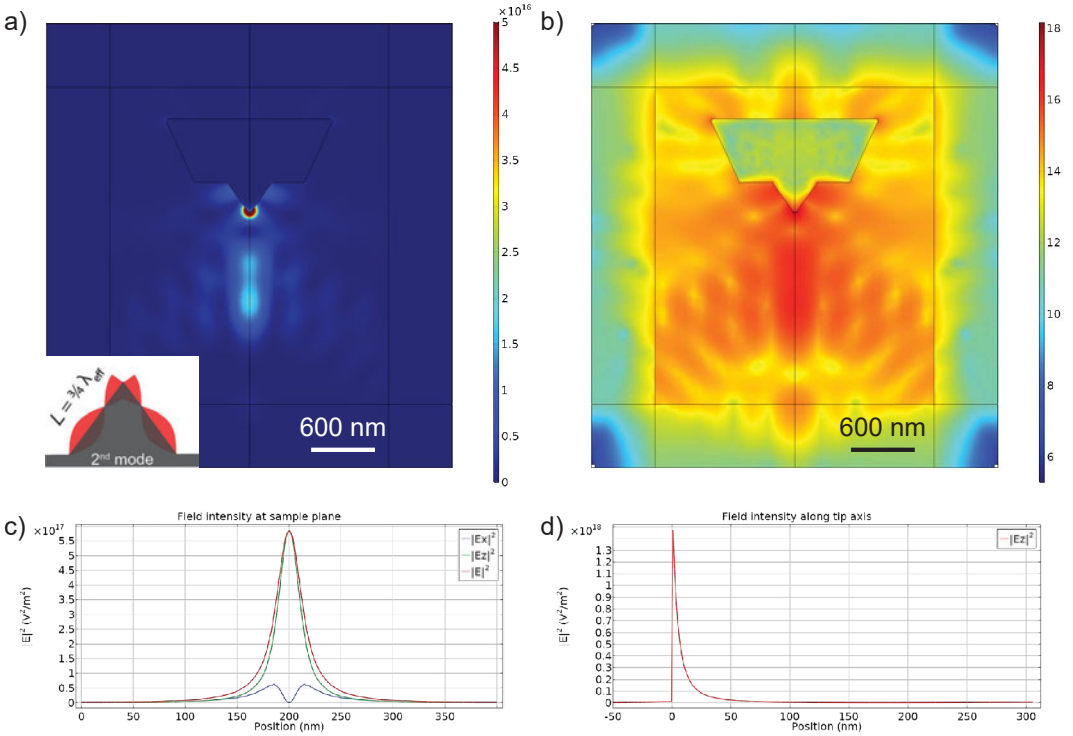

FIGURE 4.1: a) Electric field norm distribution $|E|^2$ (the inset shows a diagram of the 2^{nd} plasmonic resonance mode in the nanopyramid tip's cavity [20]); b) Base 10 logarithm of the distribution shown in a) for better inspection of low electric field intensity regions; c) distinct $|E|^2$ distributions plotted along the sample plane parallel to the plateau and 5 nm below the apex; d) $|E_z|^2$ plotted along the symmetry axis. The discontinuity at Position 0 nm is located at the transition from gold (inside the tip) to air (outside the tip).

The field distribution along the tip's symmetry axis (Fig. 4.1d)) also portrays the expected exponential intensity decay as the distance from the apex increases. This aspect will be discussed in depth in Section 4.1.4.

4.1.2 L Parameter Study

The tip's plasmonic resonance can be tuned to a particular excitation wavelength since the probe's response is a function of the nanopyramid's edge length L indicated in Fig. 3.14. Figure 4.2 (I-IV) demonstrates the dependence of the maximum $|E|$, while the blue dots in the graphics at the bottom of Fig. 4.2 shows $|E|^2$ at the sample plane located 5 nm below the probe, as a function of the tip's L parameter. For these simulations, D was fixed at 40 nm.

Conditions I, II and IV are taken on constructive resonant condition while III is taken on a destructive resonance condition. The larger intensity for the second resonante peak (II) is in accordance with experimental results [20]. Nevertheless, the $L = 470$ nm value obtained experimentally diverges slightly from the optimal 425 nm obtained in the simulations. This occurs because the present simulation optimizes for the excitation wavelength at 632.8 nm, while the experiment conducted in [20] optimizes for a compromise between excitation wavelength and graphene's Raman signal with components at 703 nm and 757 nm for G and 2D bands respectively. This highlights the importance of choosing a proper L not based only on

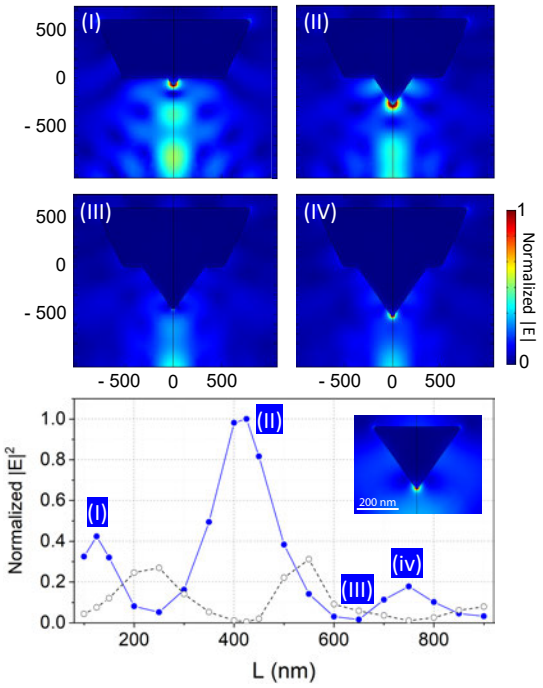

FIGURE 4.2: Dependence of maximum $|E|$ at the sample's plane with respect to L ($|E|$ is used in this case only to provide a better visualization of the distributions). Images I-IV represent the field intensity maps for the situations where L = 125, 425, 650 and 750 nm. The bottom graph shows maximum $|E|^2$ intensities for various L values under two conditions: nanopyramid with micropyramid (blue curve, closed dots) and nanopyramid without micropyramid (black dashed curve, open dots), as shown in the inset to the graph (adapted from [57]).

excitation wavelength, but also considering plasmonic resonance with the scattered signals expected from a given sample.

The optimized PTTP localized surface plasmon resonance relies both on the nanopyramid dimension and on the presence of the micropyramid plateu. The bottom graphics Fig. 4.2 also show how the performance of the tip greatly depends on the presence of the micropyramidal body associated to the nanopyramid, the curve in black-open symbols giving $|E|^2$ for the nanopyramid without the micropyramid (see schematics inset to the plot). This happens because the micropyramid acts as a mirror, generating monopole resonance modes, as opposed to the dipole mode occurring in the isolated nanopyramid [20, 23, 57].

4.1.3 D Parameter Study

The sharpness of the tip's apex, defined by the D parameter associated with the probe's apex diameter, is also critical for the electric field enhancement and the spacial resolution of TENOM images. The impact of changes to D on the resulting $|E|^2$ at the sample plane 5 nm below the apex is shown on Fig. 4.3.

The simulation in Fig. 4.3 shows a decrease in electric field amplitude and a broadening of the intensity profile as the tip's diameter increases. Consequently, larger values of D will not only affect the achievable spatial resolution in images, but

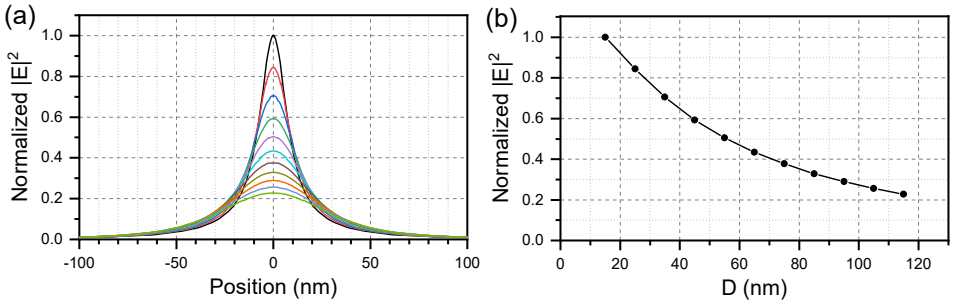

FIGURE 4.3: Dependence of $|E|^2$ as a function of D in the range $15\,\text{nm} \leq D \leq 115\,\text{nm}$. The electric field was considered at a plane 5 nm away from the probe. a) shows the $|E|^2$ profile at the sample plane; b) shows the normalized maximum field (at the 0 nm position) for the corresponding profiles. L was kept constant at 425 nm. (Adapted from [57].)

also the signal enhancement, resulting in degraded signal-to-noise ratios. To illustrate, by increasing D from 15 nm to 115 nm, the $|E|^2$ drops to 20 % and the FWHM drops to 26 % from their optimal values with $D = 15\,\text{nm}$.

4.1.4 Field dependency on sample distance

The distance between the tip and the substrate is the key parameter of TERS, responsible for the localized excitation and collection that generates nanometer resolution images, greatly affecting performance, as already hinted by Fig. 4.1d). In AFM systems, this separation between probe and sample's surface is around 5 nm for TF-based systems [3], depending on the AFM's control loop setpoint.

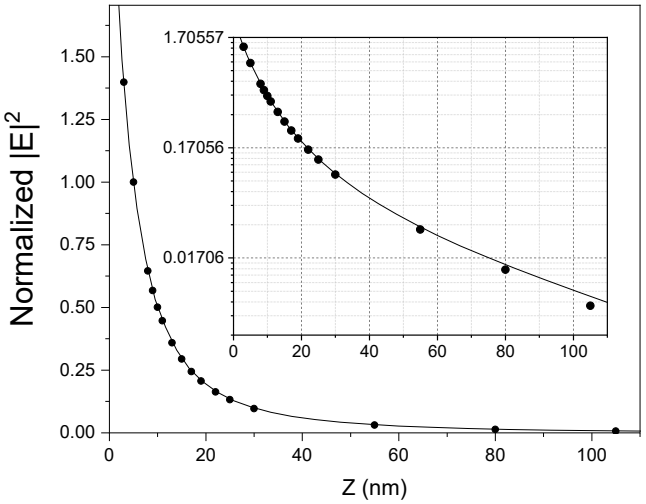

FIGURE 4.4: Simulation of the field intensity as a function of the separation between probe and sample. The line is equivalent of Fig. 4.1d), while the bullets represent the maximum intensity at the sample's plane as the tip is moved away from it by a quantity Z in nanometers. All values are normalized with respect to the value of $|E|^2$ 5 nm for the gap. The inset shows the same data in logarithmic scale. [57]

The probe-sample gap can be analyzed under two approaches: first by simply distancing the observation point away from the probe, as shown by the line-curve

in Fig. 4.4, or by moving the probe away from the substrate and focal point, corresponding to the bullets in the same plot. Interestingly, Fig. 4.4 shows that these situations are nearly equivalent, diverging only for larger separation values. The divergence (see inset) can be explained by the fact the probe is gradually moving away from the focal position, thus receiving a lower electric field excitation.

This simulation also serves as a motivation for converting TERS systems from AFM to scan tunneling microscopy (STM) based. As STM systems are known to be capable of operating safely with a gap around 1 nm, this improves signal enhancement greatly. In fact, TERS can resolve sub-nanometer features on high-vacuum STM setups [40].

4.2 Focal Region Study

As the probe-laser interaction is fundamental for the proper operation of a TERS system, it is necessary to characterize the focus region and how the metallic probe affects it. The focal spot region can be studied from three different perspectives: simulations, BCOM images and TENOM images. While the simulation approach was thoroughly explored in Section 4.1, this section is dedicated to the two other approaches, which are depicted in Fig. 4.5.

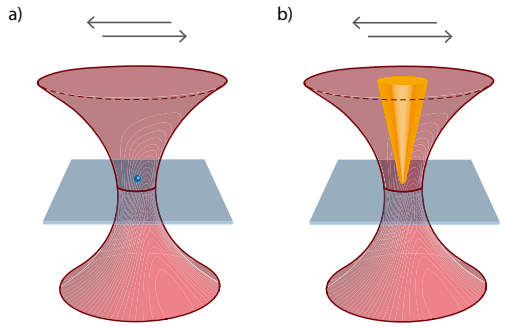

FIGURE 4.5: Confocal and TENOM approaches can be used to explore the focal region. a) The BCOM approach involves scanning the focal spot with a single molecule (moving sample) while b) the TENOM approach can be performed by scanning the focal spot with a metallic probe (moving probe). (Sourced from [18].)

4.2.1 Optical Study of Focal Spot

An effective manner to obtain the PSF of a BCOM is to scan something that resembles an impulse. This can be experimentally achieved by scanning a sample containing very bright molecules, such as the Nile Blue (NB) dye molecule, as depicted in Fig. 4.5a). In addition to assess the PSF, Nile Blue provides a visual form of evaluating the radial polarization's quality. Figure 4.6 shows in a) a single molecule image of Nile Blue with a proper radial polarization and b) was generated by misaligning the Berek compensator, effectively destroying the radial polarization.

Figure 4.6 a) determines the diffraction limited PSF. As an upright NB molecule behaves as a Z oriented dipole, it is only sensitive to the vertical component of the electric field [3]. Thus, from a different perspective, this is the field intensity distribution of the field component perpendicular to the image plane. Under this circumstance, the distance between local maximums in the Airy disk should measure

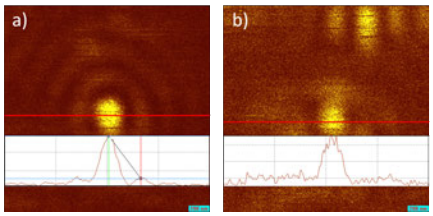

FIGURE 4.6: a) Nile blue single molecule image acquired with proper radial polarization. The lateral distance indicated by the red and blue lines, representing the distance between crest maximums, is 312 *nm*;b) Another molecule imaged with a destroyed radial polarization. In both images, the insets are the line profile intensity plot along the marked red lines.

approximately half the excitation wavelength at 632.8 *nm*. The measured value of 312 *nm* therefore deviates just 1.4% from the theoretical value of 316.4 *nm* [3].

4.2.2 Probe Study of Focal Spot

An analogous study from the previous section can be performed by scanning the focal spot with a TERS probe, since it responds predominantly to electric field excitations parallel to its axis, like the NB molecules [3]. For this experiment the PSS was used in conjunction with an exfoliated graphene sample, which acts as a spatially homogeneous Raman signal generator. In this configuration, the measured TERS intensity will be affected solely by the probe's position with respect to the laser focus.

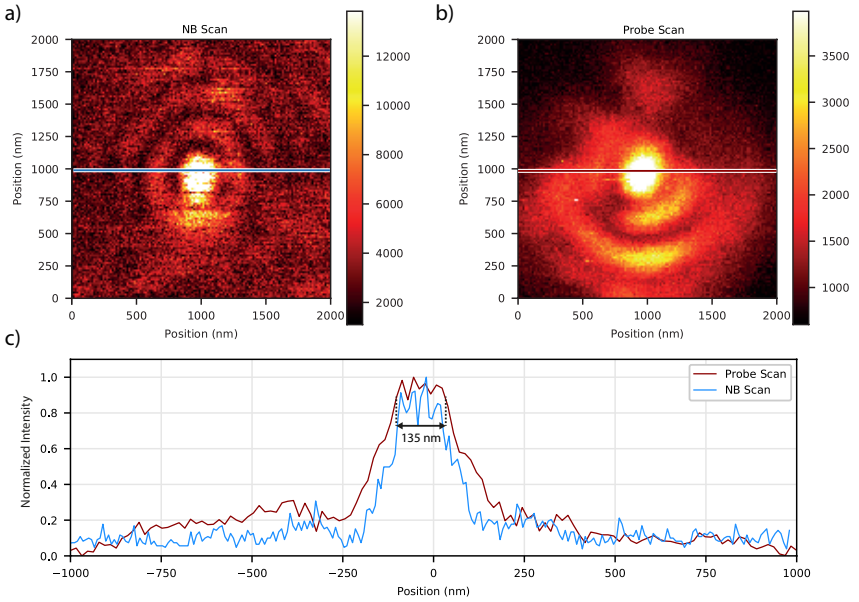

FIGURE 4.7: a) Raman map of the 2D band intensity generated by an APD while scanning the probe over graphene ; b) Luminescence mapping of a single NB molecule by an APD while scanning the sample over the focal spot (same as in Fig. 4.6 a)); c) Cross section of each map as marked in a) and b). The width indicated in c) represents the region where the signal exceeds 90 % of the maximum intensity. (Sourced from [18].)

Figure 4.7 compares both NB and probe scans. It is possible to observe that the cross section of the laser spot scanned by the PSS is larger than for the NB scan. Specifically, the FWHM of the probe scan is 236 nm and the NB scan's 203 nm. This distinction in FWHM can be attributed to the size of the scanning element, as discussed in Section 2.3, where the tip's apex size has a direct impact in the resolution of a topographic image, and in Section 4.1.3, where the impact of the apex size on the intensity profile of $|E|^2$ is shown.

Furthermore, the diameter of the central lobe or hotspot present in the probe scan is representative of the alignment tolerance between the probe and the laser spot. This tolerance is shown in Fig. 4.7c) considering a maximum signal loss of 10 %, resulting in a diameter of 135 nm. This parameter can be used as reference when developing probe alignment procedures and strategies to mitigate probe position drift over time.

4.2.3 Hyperspectral Probe Scanning

As the PSS provides the possibility to also acquire HSIs, a probe scan over a graphene sample on top of a glass substrate was performed. In this case, the HSI is able to supply information, simultaneously, regarding the G band, 2D band and luminescence generated by the tip. Figure 4.8 shows the intensity distribution for these three variables.

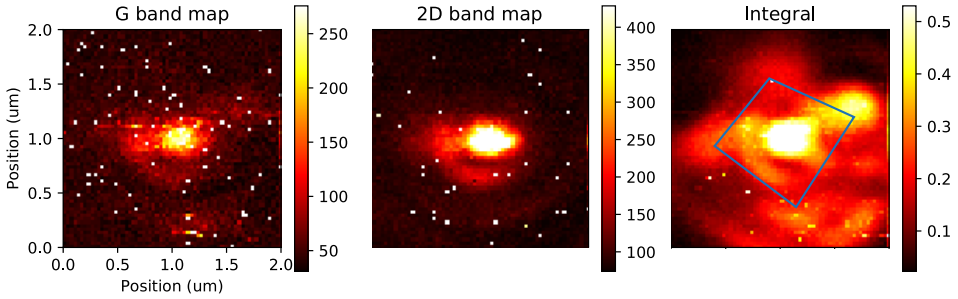

FIGURE 4.8: G (left) and 2D (middle) band peak amplitudes extracted from a HSI. The integral image (right) was generated by integrating the area under each spectrum, accounting for the contribution of the luminescent background present in the spectra. The blue overlay shows a quadrilateral pattern on the distribution of the integral image.

As expected for graphene, the G and 2D bands are colocalized, the first one having a lower intensity. Meanwhile, the integral image displays other components that are not related to the Raman effect. Interestingly, a rotated square pattern with $1\mu m$ side can be noticed in the image. This coincides with the micropyramid's plateau shape shown in Fig. 3.14.

In order to obtain a better understanding of nuances contained HSI generated by the probe scan, it's necessary to perform analysis beyond the standard band mapping images contained in Fig. 4.8. For this purpose, the spectral unmixing algorithm can be employed. Thus, the program shown in Section 3.5 was applied to obtain the four most distinct spectral signatures in the HSI and calculate their spatial distributions. The algorithm's output is shown on Fig. 4.9.

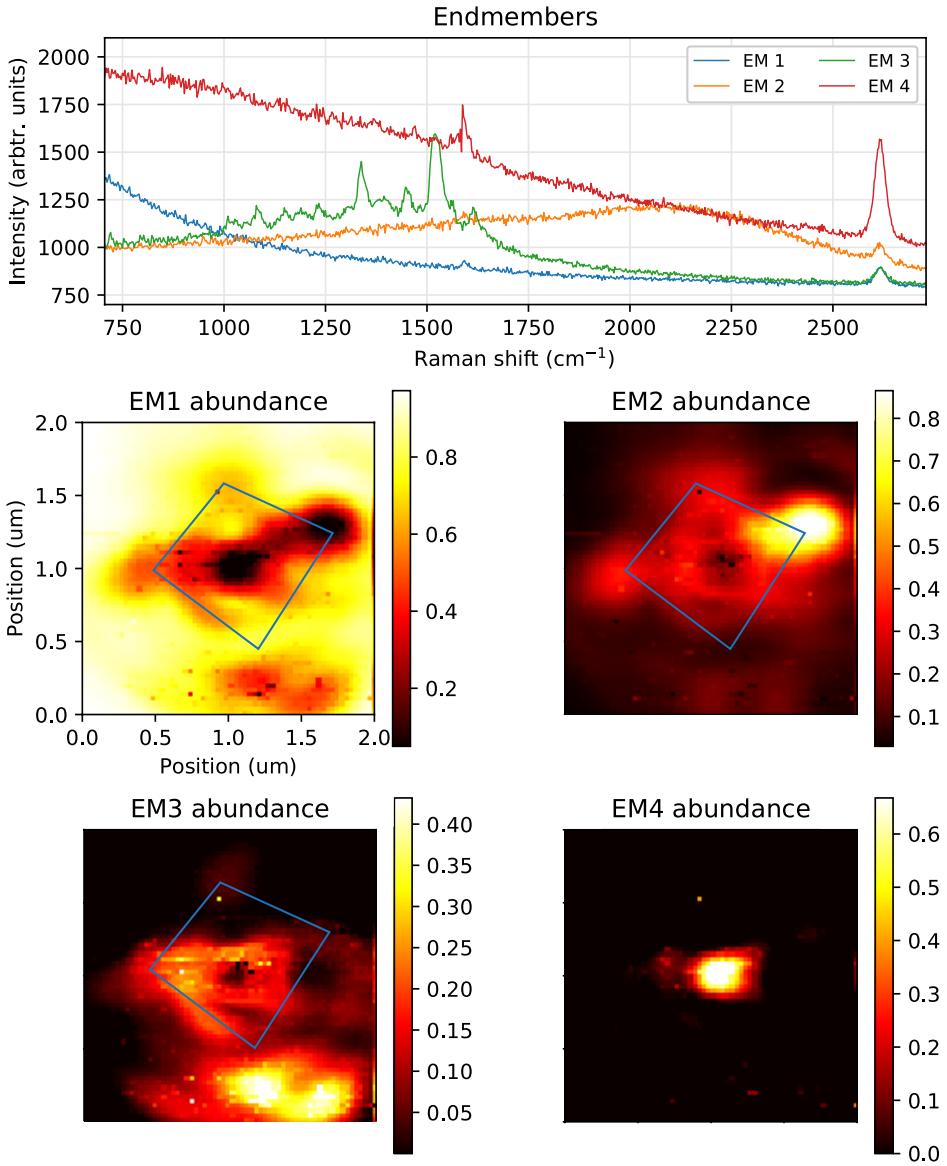

FIGURE 4.9: The endmembers graph shows the four distinct spectral signatures, denoted EM1-EM4, determined by the unmixing algorithm. The four distribution maps corresponding the abundance of each endmember in the whole scan area is also shown.

Having the spectral unmixing results, it is necessary to understand each endmember and their spatial distribution. Firstly, EM1 spectrum shows an unenhanced graphene signature summed to a background. This far-field spectrum is predominant in the HSI and is associated with a misaligned probe. EM2 also contains an unenhanced graphene component, as the G and 2D band amplitudes are equivalent to EM1. The main distinctions between EM1 and EM2 are the position and shape of the luminescent background and also the spatial distribution, which follows the blue square pattern overlay shown in Fig. 4.8. This distribution and spectral signature indicates that the vertices of the micropyramid generate a luminescence effect with a characteristic intensity profile.

Furthermore, an inspection of EM3 spectrum also does not display a significant enhancement of the 2D band while also containing a series of peaks in the lower Raman shift region which are not associated with graphene. These peaks are usually

associated with thermal damage to the probe or the sample. This aspect, combined to the inconsistent abundance map, leads to the association of this endmember with contaminants on the probe or the sample.

Finally, EM4 spectrum shows Raman signal intensity enhancement of both G and 2D bands mixed with a descending luminescent background. This aspect, combined to the narrowly localized spatial distribution, indicates that the central region in the HSI is the optimal alignment position for TERS measurements.

The colocalization of the Raman signal and the luminescence has a significant implication for the probe positioning procedure. Usually the alignment is performed manually by a technician that inspects the optical spectrum and moves the probe by means of the piezo tube. Therefore, the fact that the luminescence is colocalized with the Raman signal makes it possible to perform the alignment by only inspecting the APD's signal intensity in a wavelength where the luminescence is significant. Since APDs in general are much faster than spectrometers and the luminescence is much more intense than the Raman signal, one can establish a fast optical feedback loop to properly position the probe. Still, care must be taken with regions of local maximum.

Alternatively, advancements in efficiency for spectrometers proportioned by electron multiplying CCDs , EMCCDs, enable the acquisition of fast HSIs around the focal region. This enables a fast exhaustive search of the focal region for the maximum intensity region, which can be clearly isolated via spectral unmixing as shown in this Section.

4.2.4 Field Intensity Distribution for Force Mapping

Having an understanding of the interaction between probe and laser focus, it is possible to propose an alignment procedure more efficient than the current method. The present process consists of visually inspecting the optical spectrum, analyzing enhancement, while manually changing the XY probe position via the piezo tube contained in the scanhead via the software interface shown on Fig. 3.6. This procedure requires user expertise, it is time consuming and prone to error, as the focal region depicted in the Section 4.2.3 presents local maxima that can mislead the operator.

A proposed system to mitigate this difficulty is to supply the operator with an NMS with optical feedback, as described in Section 3.4. One of the key aspects of this system is the force mapping, described by Eq. (3.2). In this subsection the simulation of the force maps generated by these equations in conjunction with experimentally acquired probe scan images will be studied. The simulations for all the predefined force types with different aggressiveness, A, factors are displayed.

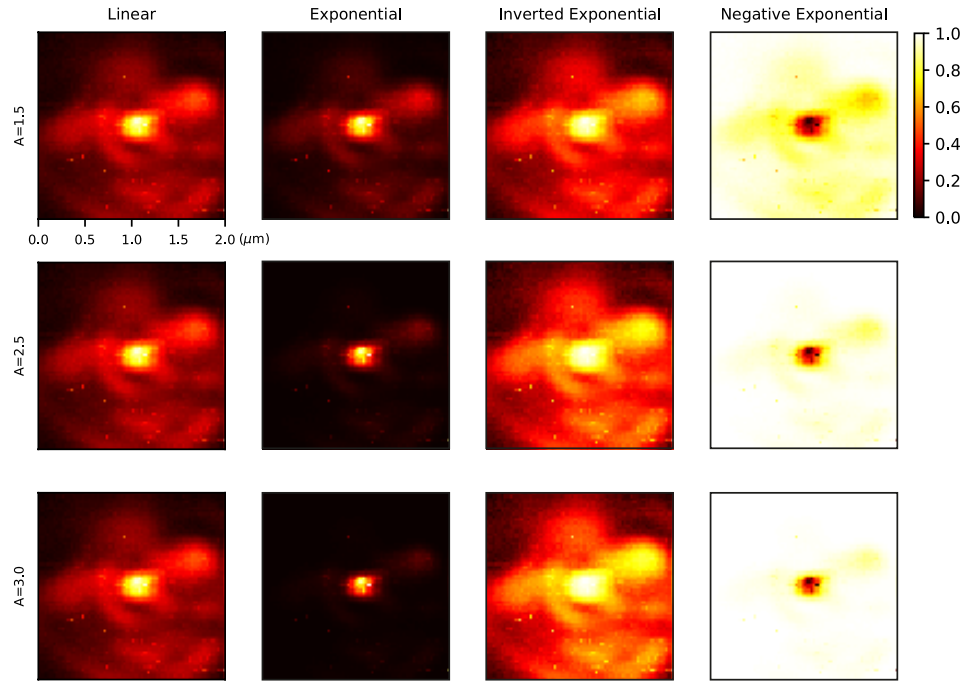

FIGURE 4.10: Simulation of force mapping based on Eq. (3.2) and using the integral image from Fig. 4.8 c) as a base for calculation. The columns contain the calculations for each force type and the rows hold the results for $A = 1.5,\ 2.5,\ 3.0$. In the images, the brightness of the pixels is proportional to the force amplitude for when the probe is positioned over that position.

The linear force type can be used if the operator only desires to adjust the overall sensitivity, without changing the shape of the force map. In contrast, the exponential mapping changes the force map generating a much higher positive force for regions of high optical intensity. The downside of the exponential mapping is that it flattens the regions of relatively low signal. The inverted exponential results in a flattening of the higher intensity region in the center of the map, but it provides better contrast for the regions of low intensity. This transformation enables te operator to have some feedback signal despite being significantly far from the optimal alignment condition. Furthermore, the negative exponential mapping is equivalent to the exponential but with opposite force direction. The negative exponential might be preferable from the positive one, as the haptic arm's mechanical resistance will decrease as the operator moves towards the optimal position.

4.2.5 Dependency of Focal Spot on Focus Plane Condition

The shape and intensity of the focal spot can vary significantly depending on the distance between the objective lens' focal plane and the sample plane. This effect must be properly understood in order to determine the optimal focus condition for the conduction of TERS experiments. To study this effect, successive probe scans were performed while varying the objective lens' focal plane, as shown on . The initial position for the experiment was for an optimized condition for Raman signal on a graphene sample without the presence of the TERS probe. From this initial condition a scan was performed obtaining the result for Position 0 in Fig. 4.12. In sequence, the focal plane was shifted up in two equal steps of 300±100 nm, generating Position 1 and Position 2 images. The focal plane was then brought back to the initial condition

and another scan was performed to validate the focal plane's return, as the objective lens positioning system is open-loop. The focal plane was then shifted downwards, away from the tip, obtaining Position -1 and Position -2 images.

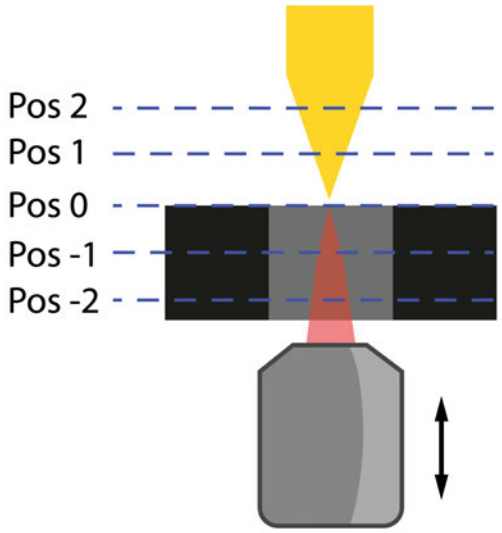

FIGURE 4.11: Schematic for the procedure of successively scanning different Z planes around the focal position. The objective lens is progressively moved up or down and, for each position, a probe scan is performed. Note that the vertical position of the probe does not vary throughout this experiment.

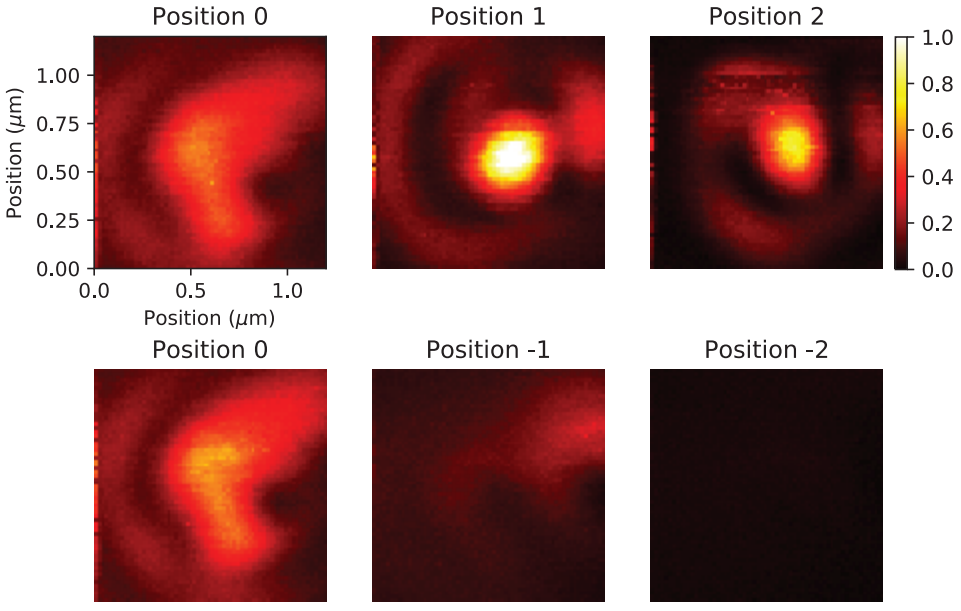

FIGURE 4.12: Successive probe scans performed on graphene's 2D band while varying the objective lens' position between Positions 0, 1, 2, 0, -1 and -2. Position 0 was obtained by optimizing the Raman signal on a graphene sample without the tip. Positions 1 and -1 are equidistant from Position 0, but the first is located above the sample plane and the second below the sample plane. The same happens for Positions 2 and -2. (Sourced from [18].)

TABLE 4.1: Intensity statistics for probe scans taken while varying focal condition. Minimum and maximum values are given in CCD counts.

	Min	Max	Ratio
Pos 0	3,610	19,220	5.32
Pos 1	2,800	33,810	12.01
Pos 2	1,380	24,500	17.75
Pos -1	2,420	10,250	4.24
Pos -2	1,300	2,330	1.79

A few metrics of interests regarding the scans under different focus conditions are summarized in Table 4.1. The table quantifies the significant enhancement increase that occurs when shifting the focal spot towards the tip. On Position 2, approximately 600 nm above the sample plane, the signal to noise ratio is 3.33 times higher as a consequence of an increased intensity for the hotspot accompanied by a reduction in the background intensity associated with the far-field signal.

Alternatively, for Positions -1 and -2, where the focus is positioned below the sample's plane, the signal falls drastically as a result of moving away from not only the sample but also from the tip.

These observations are consistent with already established theory that the main interaction series for TERS is Tip-Sample-Tip (TST) sequence: first the excitation light interacts with the probe generating a nanometric light source that shines on the sample, producing the Raman scatter effect, which is then collected by the probe and converted and enhanced by the probe producing a propagating electromagnetic signal [3]. Therefore, it is expected that exciting the probe will favor the TST sequence, resulting greater signal to noise ratios.

In essence, the present experiments provide an important guideline for TERS measurements performed under similar illumination and collection configurations, as the current experimental setup descripbed in Chapter 3. The tip-laser alignment must include a shift upwards for the objective position as to properly excite the nanopyramid body producing larger enhancements and lower background intensities.

4.3 Impact of Substrate on TERS

So far the focus of the work was aimed at the probe and its interaction with the focal spot. Nonetheless, another key aspect to be taken into consideration is the composition and features of the substrate over which the analyzed sample is positioned. For instance, the use of a metallic substrate (configuring a gap mode due to the significant electric field confinement provided by the two metallic structures) can further enhance the local electric field between the probe's apex and this substrate due to gap-plasmon resonance that occurs in this configuration [60]. Furthermore, the presence of inhomogeneous metallic structures in the substrate can also have interesting effects in the electric field distribution. This is, in fact, the basis of the surface-enhanced Raman spectroscopy (SERS) [61]. The combination of SERS and TERS creates interesting phenomena that can affect spatial resolution significantly, as it will be shown further in this section.

4.3.1 Technical Aspects

For this study, three different samples were produced in order to tailor the electic field to distinct configurations: (i) conventional microscopy glass coverslip (Fisher Finest Cover Glass); (ii) homogeneous 12 nm thick gold film thermally evaporated over a coverslip; (iii) regular distribution of gold nanoparticles (AuNP) with $12(2)$ nm stabilized by oleylamine molecules providing a separation of approximately 10 nm between particles, as shown in Fig. 4.13. Samples (ii) and (iii) are courtesy of Dr. Patryk Kusch from Freie Universität Berlin and are further documented on Refs. [56, 62] respectively.

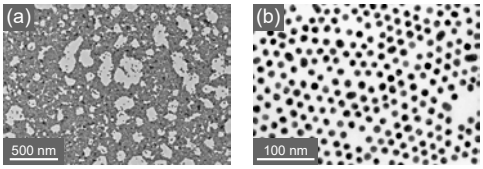

FIGURE 4.13: SEM images for substrate (iii) containing the oleylamine-stabilized gold particles under two distinct magnifications. The particles self-assemble to a rough hexagonal pattern due to the oleylamine molecules which are not visible in the images. (Sourced from [56].)

Graphene was mechanically exfoliated on top of each of these substrates as to provide an homogeneous Raman scatterer to be measured using TERS. The three samples were scanned using a same PTTP with $40(10)$ nm diameter provided by Inmetro.

4.3.2 Non-gap and Gap Mode Simulations and Experiments

As shown in Fig. 3.14, the simulation setup is fitted with a region on top of the glass substrate that enables the simulation of thin films. This feature is used in order to simulate the configuration of the electric field for substrates (i) and (ii), the glass and gold film substrates respectively. When the thin film region is composed of gold, a gap mode configuration is achieved, whereas a non-gap mode configuration can be achived by using glass in this region. Since glass is a dielectric material, it does not provide a strong electric field confinement, characteristic of the gap mode. Figure 4.14 displays the electric field configuration at the subtstrate's surface for glass and gold while also distinguishing between horizontal (X) and vertical (Z) components.

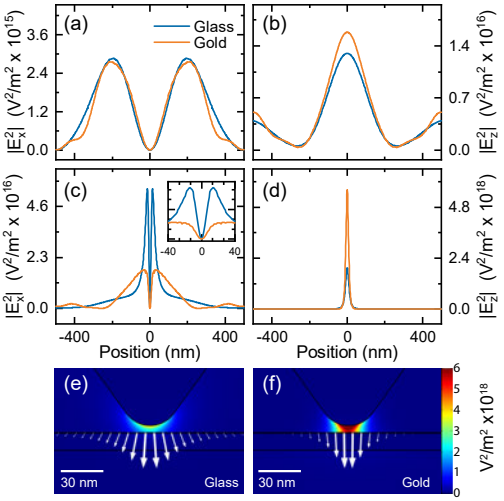

FIGURE 4.14: Simulated intensities of $|E^2|$ at the sample plane for glass and gold substrates. Graphs (a) and (b) show horizontal and vertical component intensities in the absence of the tip, while (c) and (d) show the respective results now in the presence of the TERS tip. Panels (e) and (f) show the electric field intensity distribution on a 2D plane section around the probe's apex with white arrows indication field orientation at the sample's plane. (Sourced from [56].)

In the absence of the metallic tip, the electric field distribution at the sample's plane is fairly similar for glass and gold film substrates, as show in Fig. 4.14a) and b). When the tip is introduced,in Fig. 4.14c) and d), all distributions get more localized due to the antenna effect produced by the probe. Notably, for the horizontal component, the distribution is more intense and localized for glass than gold, as shown in Fig. 4.14c) and its inset. This trend changes for the vertical component distribution, where the electric field distribution for the gold film case is 70 nm more intense and 26 nm narrower than for the non-gap mode. It is also important to note that, when comparing horizontal and vertical components, there is a two orders of magnitude difference between the distribution intensities. Considering that the measured TERS signals are proportional to $|E^4|$ [63], the vertical component can have a more significant contribution to the measured signal, but the actual contribution also depends on a material's Raman tensors, as discussed in Section 2.2.

Another manner of evaluating the electric field configuration for non- and gap mode configurations is to perform probe scans around the focal region. Such experiments were performed and the resulting 2D band Raman intensity maps are shown in Fig. 4.15.

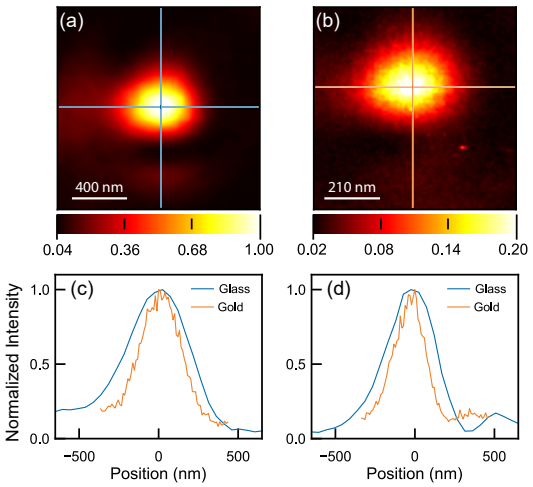

FIGURE 4.15: Probe scanning measurements for glass and gold film substrates. Maps a) and b) present the 2D Raman band intensity map for glass and gold cases, respectively, both normalized by the maximum intensity in a). Graphs c) and d) show horizontal and vertical cross-sections of these maps, now with all intensity profiles normalized independently. (Sourced from [56].)

As both images were acquired using the same probe on the same system, the variable that provides the difference between the two scans is the substrate. There are key differences in signal intensity and measured width for the laser's hotspot. The maximum intensity for the gold film scan was 20 % the central intensity of the glass scan. This is consistent with the simulations indicating that the field is more concentrated in the direction perpendicular to the substrate when on gap mode. As graphene responds poorly to this kind of excitation, the Raman signal decreases, even though the vertical component of the excitation is more intense for the gap mode. Regarding the width of the hotspots, the FWHM of 429 nm for glass and 291 nm are also consistent with the simulations, which indicate a narrower electric field distribution for the gold film configuration.

These particularities for each substrate draw attention to the importance of choosing the a substrate that is adequate for measuring a given material. For example, as graphene responds poorly to excitations perpendicular to its plane, gap mode is not recommended when trying to maximize the measured Raman signal. In the other hand, as the near-field response in this condition is narrower, gap mode will result in a slightly improved resolution. Therefore the measured material and a given experiment's goals must be taken into consideration when choosing the adequate substrate.

4.3.3 Effect of Substrate on Spectral Enhancement

This section expands on the observations made in the previous one regarding the difference in signal intensity in graphene samples on top of different substrates. Figure 4.16 brings a comparison between tip-down (near-field plus far-field) and tip-up (fa-field only) graphene spectra combined with the three types of substrate described in Section 4.3.1.

TABLE 4.2: Spectral enhancement for G and 2D graphene bands on the three substrate types.

	Glass	Au film	AuNP
G	10 ± 4	7 ± 1	5 ± 3
2D	16 ± 1	5 ± 1	5 ± 1

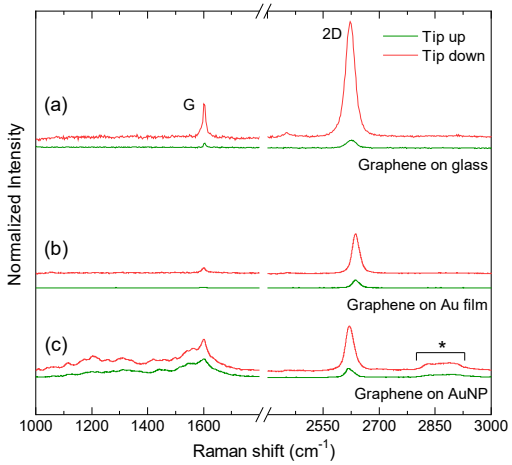

FIGURE 4.16: Near- and far-field signal comparisons on three different substrates. All pairs are normalized with respect to the 2D band intensity in the tip up condition. The marked signal in c) represents the spectral signature of the oleylamine molecules used to stabilize the AuNP. (Sourced from [56].)

For each of the six situations represented in Fig. 4.16, seven spectra were selected and averaged to obtain Table 4.2 summarizing the spectral enhancements and uncertainties for each Raman band and substrate. The spectra were obtained during a scanning procedures in homogeneous regions in each of the substrates with accumulation time per spectrum of 2 s for glass, 5 s for Au film and 10 s for AuNP. All data was acquired with an excitation power of 160 µW measured at the sample.

Due to the change in electric field orientation at the sample's plane for gap mode, lower enhancement levels were expected overall for the Au film substrate (gap mode). Nonetheless, a discrepancy arises when comparing the loss of spectral enhancement for the G and 2D bands from Glass to Au film substrate. G band's enhancement suffered a 30 % loss while the 2D band suffered a 69 % loss. This discrepancy can be explained by group theory and is discussed at length in Ref. [56], beyond the scope of this work. The similarity in enhancement of the G and 2D bands in the AuNP substrate can be varying electric field distribution during the scan, as will be discussed in Section 4.3.4.

4.3.4 Effect of Substrate on Spatial Resolution

So far the focus has been on how the substrate affects the electric field distribution at the sample's plane and how this, consequently, affects spectral enhancement. However, the substrate composition and shape may also affect the spatial resolution. This was already briefly discussed when comparing the probe scanning results in Fig. 4.15 where the intensity distribution for the Au film was measured to be narrower than for a plain glass substrate, which will directly impact the spatial resolution of the system. This occurs because the PSF of imaging system in the gap-mode

configuration is narrower, and this has direct impact on the highest possible spatial frequency that can be resolved by the imaging system.

Not only a narrower PSF can affect the spatial resolution of images generated by a given system, but if the PSF changes as a function position during the scanning procedure, the spatial resolution is also altered. This is the case for a structured gap-mode substrate such as a surface covered with AuNP like in substrate (iii). Simulations depicted in Figure 4.17 illustrate how the configuration of the electric field changes as the substrate moves underneath the tip's apex. It is important to note that the simulation environment had to be reduced here due to computational costs, as the moving substrate breaks the symmetry that enables the reduction of the 3D simulation space. Despite the dimensionality reduction, all other properties described in Section 3.6 still hold, except for the substrate which is composed now of 12 nm AuNP particles with a gap of 10 nm between particles. The substrate contains 50 of such AuNPs and the sample's plane was place 0.1 nm above the top portion of the particles to avoid artifacts.

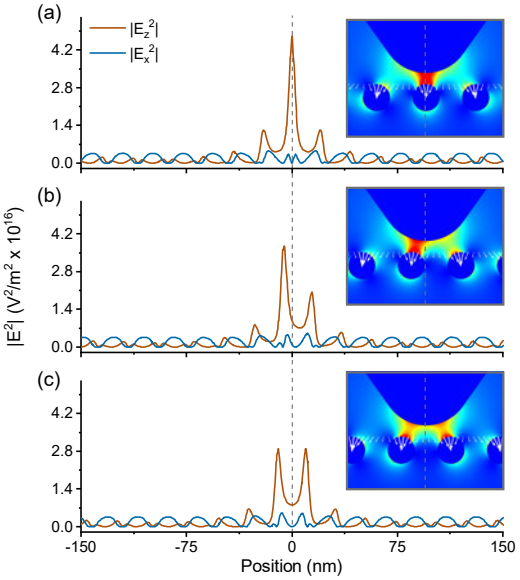

FIGURE 4.17: 2D simulation of changes in horizontal (X) and vertical (Z) components distribution as a set of AuNP is translated underneath the tip's apex. The white arrows in the insets indicate electric field orientation at the plane where graphene would be located. (Sourced from [56].)

Figure 4.17 shows how the vertical component $|E_z^2|$ is more pronounced when a particle is exactly underneath the tip than when the probe is placed in-between particles. Interestingly, the $|E_x^2|$ component is largely unlocalized with multiple local maxima with similar amplitudes, independently of AuNP positions.

The experimental equivalent of this simulation was also performed by a 120 nm long scan in substrate (iii), a relatively small region when considering the probe's apex radius of 40 nm.

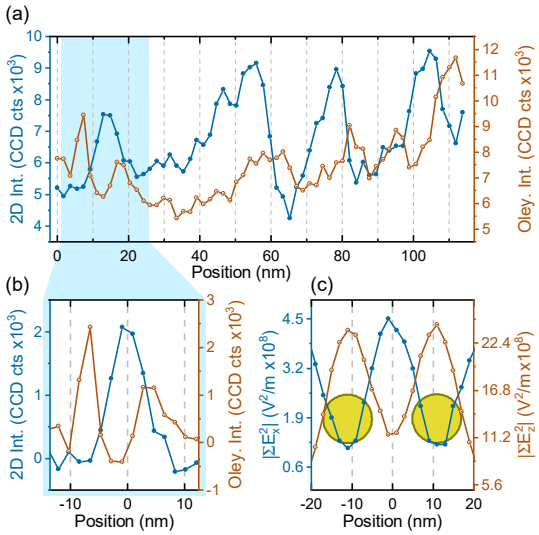

FIGURE 4.18: Line section of a scan performed on a AuNP substrate. a) shows the intensity profile for the graphene's 2D band in blue and for oleylamine's Raman band in yellow (spectra acquired with 160 µW excitation power and 2.5 sec integration time per point.); b) zoomed detail of the highlighted section in a) with linear trends removed for better visualization; c) simulated intensities for discretely integrated in-plane (X, blue) and out-of-plane (Z, yellow) electric field components during a line scan. The gold circles indicate the position of the AuNP in the simulation space. (Sourced from [56].)

The measured spatial resolution for the 2D band modulation in the scan from Fig. 4.18 is 6.8 nm, which is close to the Nyquist limit of 3.75 nm considering the size of each pixel being 1.875 nm (the 120 nm scan length was sampled 64 times). This measured spatial resolution can be considered a "super-resolution" as the probe's apex radius of 40 nm would not be able to provide such resolution under normal conditions.

Additionally, Fig. 4.18a) also shows different trends for the graphene's 2D band intensity and the oleylamine's band (indicated in Fig. 4.16) intensity. Figure 4.18 highlights these trend differences, as the oleylamine's signal decreases, the 2D band signal increases. This dynamic is explained by how the electric field summed along the sample plane varies as the AuNP move underneath the tip. The in-plane (X) excitation is larger when the probe is in-between particles, favoring the Raman scattering for the graphene 2D band, and the out-of-plane (Z) excitation is larger when the probe is on top of a particle, favoring the excitation of the oleylamine molecules coating the AuNP.

The reported experiments and simulations successfully predict and demonstrate how super-resolution can be obtained with a strategic choice of substrate, resulting in Raman signal modulations with spatial frequency exceeding the dimension of the tip's apex. This measured resolution, however, must be interpreted with care. When comparing the electric field distribution for the AuNP sample in the tip up and down conditions, as illustrated in Fig. 4.19, the lack of field localization becomes clear, specially for the in-plane component.

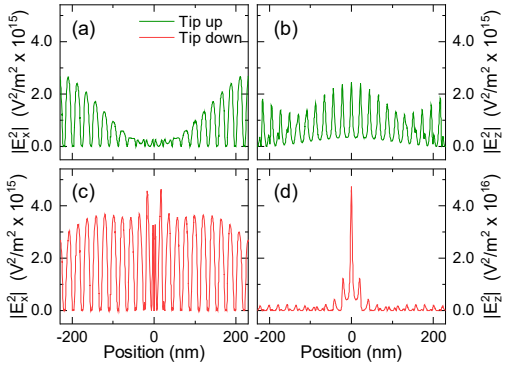

FIGURE 4.19: Comparison of electric field distribution in the tip-up (far-field) and tip-down (far-field plus near-field) configurations for in-plane (X) and out-of-plane (Z) components, measured 0.1 nm above the top of the AuNP. (Sourced from [56].)

The lack of electric field localization means that the signal measure for a given pixel during a scanning sequence does not come exclusively from the immediately neighboring region, but from a region that can comprehend hundreds of nanometers. This is a key insight for understanding experiments performed under simular conditions.

4.4 PCA for Feature Extraction

PCA can be used to improve the effectiveness of a K-means clustering algorithm for classifying graphene in terms of number of layers.

The dataset used consists of a HSI containing regions with graphene with different numbers of layers, which are not initially known. The only pre-processing executed was the removal of outliers and subtraction of the mean spectrum from all datapoints.

Figure 4.20 a) and b) are images of the intensities of two specific graphene Raman bands, G and 2D respectively. Usually the shape and intensity ratio of these two bands are used to determine the number of layers [14]. The issue is that to extract accurately the necessary information one must execute a fitting procedure which is non trivial, specially for the 2D band which can be composed by up to 5 Lorentzian functions [13], requiring human inspection to validate the fitting result.

In this circumstance, an approach using PCA is proposed. Given this dataset, a PCA transformation was executed and the first three PCs, accounting for 56% of the explained variance were used. This choice was taken in order to be able to directly visualize the data, as in Fig. 4.20 c) and d). The 3D plot shows a tetrahedral shape, indicating that there are four types of spectral signatures in the data. The weights given by the PCs are able to provide hints of the features that were automatically extracted from the spectral signatures. e) has the peak ratio characteristic of graphene with many layers. Meanwhile, f) have different signed intensities for the G and 2D bands, which can be related to a measure of peak intensity ratio between the two bands. Furthermore, g) has a deformed 2D peak that is able to extract distortions in its shape that are directly related to the number of layers.

The spectral signatures for the vertexes of the tetrahedron shows the distinct classes of materials the algorithm isolated. h) is the typical signature of a bilayer graphene, i) represents the substrate background, j) indicates three or more layers and k) is the signature of monolayer graphene.

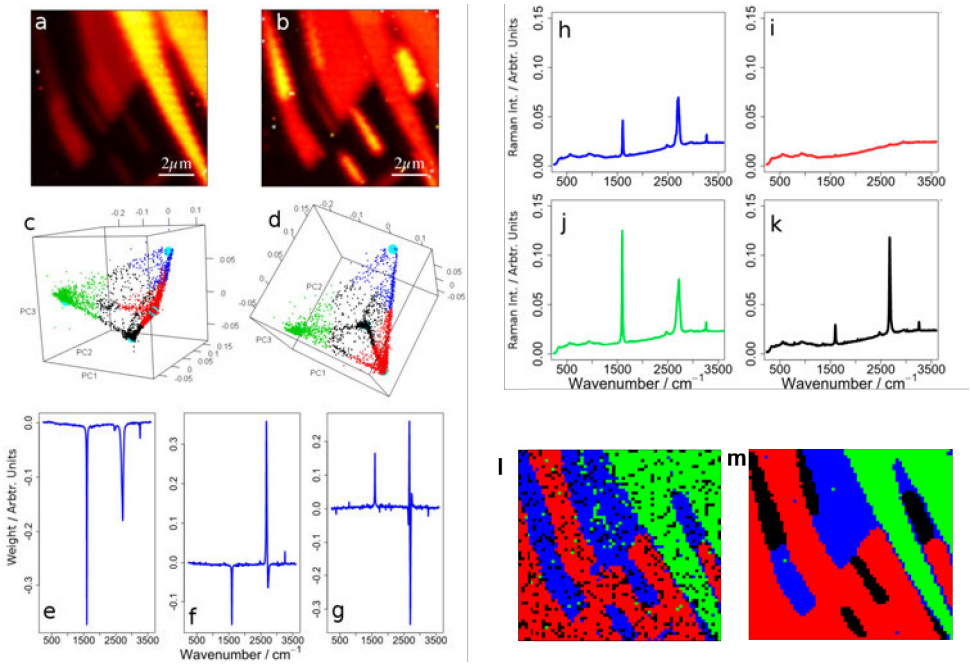

FIGURE 4.20: a) and b) are the G and 2D band images extracted from the HSI of a graphene sample deposited on a SiOx substrate; c) and d) are 3D visualizations of the PC space generated by the three most meaningful components that account for 56% of the total variance; e), f) and g) are the weights for these components; h), i), j) and k) are the representative spectra for the center of each of the four clusters found; l) is the same image as in a) artificially colored based on corresponding cluster based on raw spectra data, and m) is the same as l) but using the first 3 PCs as features. (Adapted from [36])

The feature space in this problem was reduced 341 times in this example, since the raw spectra have 1024 features and only three components were used. Nevertheless, this reduced feature space is able to produce better clustering results, as shows in Fig. 4.20 l) and m).

4.5 Spectral Unmixing

Spectral Unmixing can be used as an effective tool for HSI exploration. To showcase its potential a sample of isolated graphene nanoflakes was scanned in order to obtain an HSI to offer as input for the algorithm. The only pre-processing done in the data was the removal of the effect of the cosmic rays.

A preliminary analysis of the image, using the same method as of Fig. 4.8 for generating G and 2D band images, results in two similar images of isolated bright regions were the graphene nanoflakes are located. A visual inspection of Fig. 4.21 does not show any significant differences between the two band maps.

Nevertheless a spectral unmixing analysis of the same dataset can potentially reveal additional information, as it processes the whole spectral range, not only specific narrow ranges chosen *a priori*. The unmixing algorithm results are shown in Fig. 4.22. The procedure was able to isolate a single nanoflake, near the center of the image, representing it with the EM 2 signature. The spectrum of this endmember is compatible with amorphous carbon and, since it contains a G band it appears on the G band map, possibly leading to the conclusion that it is, in fact, a graphene

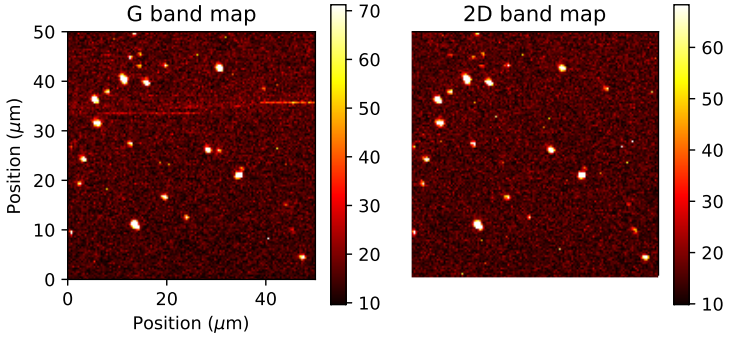

FIGURE 4.21: G and 2D band images of isolated graphene nanoflakes.

nanoflake. The only previous indicator of the presence of amorphous carbon in the sample is the absence of this particular bright dot in the 2D band image, but the unmixing algorithm was capable of clearly outlining its presence with the only user input being the number of endmembers to use for the algorithm.

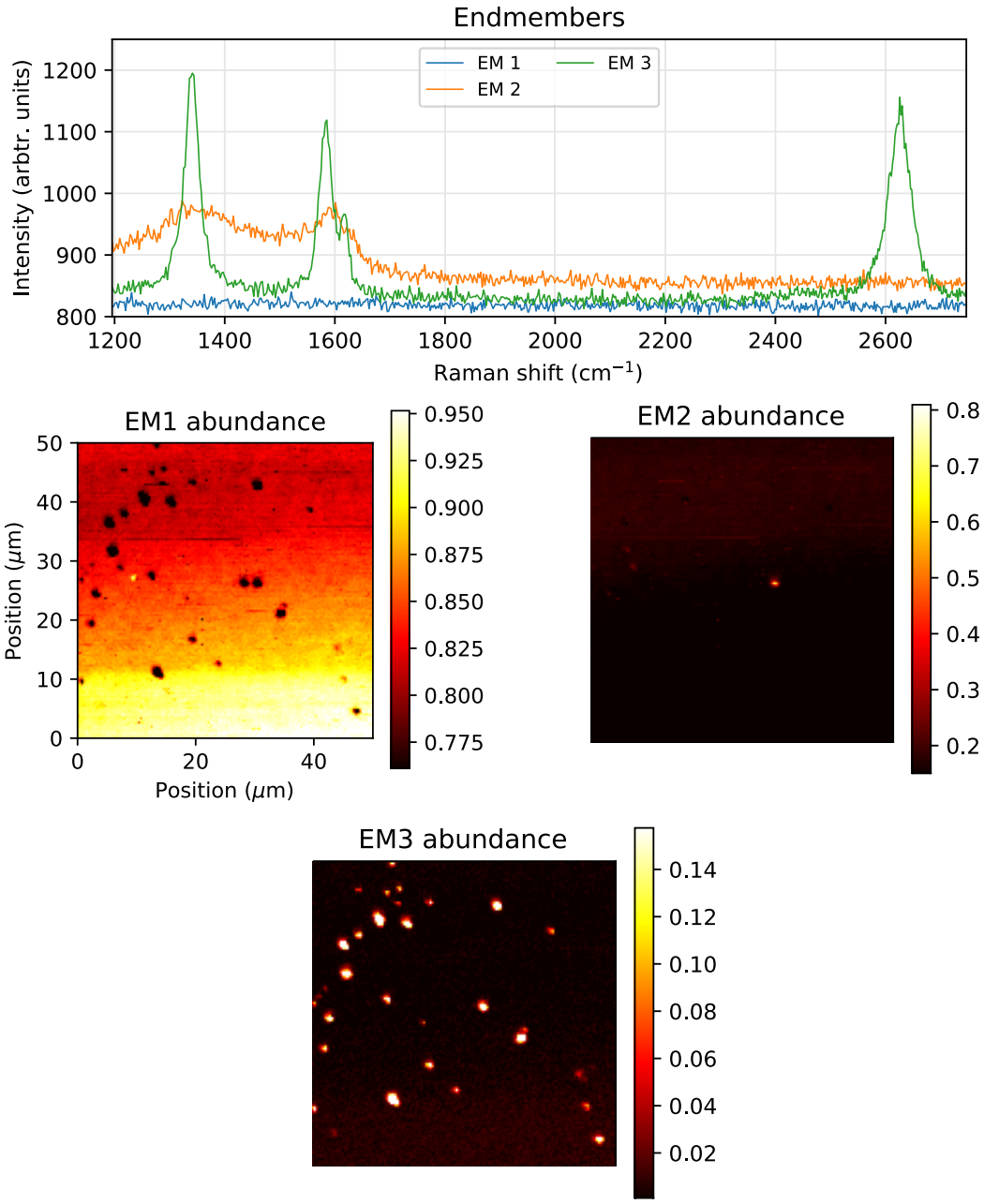

FIGURE 4.22: Spectral unmixing analysis with three endmembers of the dataset presented on Fig. 4.21. EM 1 presents a typical background signature; EM 2 presents an amorphous carbon fingerprint; EM 3 shows a signature of a highly defective graphene, which is usual for flakes of nanometric size.

Chapter 5

Conclusion

The developed work consisted of three main fronts: tooling development, Raman spectroscopy experiments and data analysis.

On the tooling front, the PSS was successful in obtaining probe scan images, which were the basis of the focal spot analysis and could also be used for an automatic probe alignment procedure. This tool is a significant improvement on the classical manual alignment method, as it not only serves as an alignment tool, but can also provide measures of quality pertaining the optical system and the probe itself. The NMS, despite only presenting preliminary results, is a promising approach for the alignment procedure, as it does not require a full scanning of a region. Furthermore, the provided flexibility of choosing a feedback signal and a force mapping rule can be of much intereset for a range of nanomanipulation applications.

Furthermore, still on the tooling front, the finite element simulation apparatus developed in this work was shown to be an efficient tool to assist the design of TENOM probes as one can rapidly prototype new probe geometries and materials while analyzing their response. The simulation tooling has also proven useful to understand experiments under different conditions, specially regarding distinct substrates other than standard glass. In addition, the efficient formulation of the simulation environment allows for the execution of simulations in desktop computers.

The TERS and Raman spectroscopy experiments revealed interesting aspects on how graphene responds under different conditions, while also showcasing its capacity for being a TERS prototyping material. The experiments also showcase the applications of the toolset that was developed in this work. The new tools, specially the PSS and simulation environment, have proven of great importance in complementing the TERS theoretical background and successfully explaining experimental results.

Finally, in terms of data analysis, two solutions were presented: PCA and spectral unmixing. Both have been proven to be efficient exploratory tools for HSIs. The dimensionality reduction provided by these techniques provide, with minimal user input, non-trivial information regarding complex datasets. Additionally, the spectral unmixing solution, whose theoretical background was developed in the scope of this work, has already been made available to Raman spectroscopy users in general and is thriving is assisting in data exploration. These tools empower physicists, biologists, chemists and others in generating more meaningful insights on hiperspectral data generated in their experiments.

Many of the findings produced throughout the work, in addition to the developed toolset, are being incorporated in a commercial, nationally produced, TERS equipment to be launched in 2021.

5.1 Future Work

The future work will consist mainly of utilizing the tools presented in this work to further improve the technology of commercial TERS systems and probes. Possible contributions are:

- To create a standalone application for probe simulations - The Comsol software utilized in this work provides the option of creating user-friendly standalone applications based on simulation environments. The finite element simulation framework for TERS probes proposed in the document can thus be polished for this purpose and distributed to physicists focused on studying and optimizing TERS probes for different purposes;
- Tip-laser alignment - This work provides the necessary background for elaborating a routine for automatic probe alignment for TERS experiments. It is now possible to propose a safe alignment routine that can be incorporated in commercial TERS systems;
- Reference samples for TERS - The insights provided in this work on how the excitation electric field influences TERS measurements could be used to elaborate a reference substrate that can be utilized to characterize a TERS system's lateral resolution and spectral enhancement.
- NMS - Integrate the nanomanipulation system to a commercial TERS setup at hardware and software levels in order provide new functionality for tip alignment and sample manipulation.

Appendices

Appendix A

Published Work

Parts of the research presented in this document have already been made public through the following media:

- *Journal Paper* - **MIRANDA, HUDSON**; RABELO, CASSIANO ; VASCONCELOS, THIAGO L. ; CANÇADO, LUIZ GUSTAVO ; JORIO, ADO . Optical Properties of Plasmon-Tunable Tip Pyramids for Tip-Enhanced Raman Spectroscopy. Physica Status Solidi. Rapid Research Letters (Internet), v. NA, p. 2000212, 2020.

- *Journal Paper* - **MIRANDA, HUDSON**; RABELO, CASSIANO ; CANÇADO, LUIZ GUSTAVO ; VASCONCELOS, THIAGO L. ; OLIVEIRA, BRUNO S. ; SCHULZ, FLORIAN ; LANGE, HOLGER ; REICH, STEPHANIE ; KUSCH, PATRYK ; JORIO, ADO . Impact of substrate on tip-enhanced Raman spectroscopy: A comparison between field-distribution simulations and graphene measurements. Physical Review Research, v. 2, p. 023408, 2020.

- *Journal Paper* - CAMPOS, JOÃO LUIZ ELIAS; **MIRANDA, HUDSON**; RABELO, CASSIANO; SANDOZ-ROSADO, EMIL; PANDEY, SUGANDHA; RIIKONEN, JUHA; CANO-MARQUEZ, ABRAHAM G.; JORIO, ADO. Applications of Raman spectroscopy in graphene-related materials and the development of parameterized PCA for large-scale data analysis. JOURNAL OF RAMAN SPECTROSCOPY, v. 48, p. JRS5225, 2017.

- *Complete Work in Conference Proceedings* - **MIRANDA, HUDSON**; RABELO, CASSIANO ; VASCONCELOS, THIAGO L. ; CANCADO, LUIZ GUSTAVO ; JORIO, ADO . Study of the interaction between light and nanoantennas in Tip-Enhanced Raman Spectroscopy. In: 2019 4th International Symposium on Instrumentation Systems, Circuits and Transducers (INSCIT), 2019, Sao Paulo. 2019 4th International Symposium on Instrumentation Systems, Circuits and Transducers (INSCIT), 2019. p. 1.

- *Abstract in Conference Proceedings* - **MIRANDA, H. L. S.**; RABELO, CASSIANO; CAMPOS, JOÃO LUIZ ELIAS; JORIO, ADO. Estudo de imagens hiperespectrais por meio de decomposição espectral e PCA. 2017. (Poster presentation, V Encontro Brasileiro de Espectroscopia Raman).

- *Abstract in Conference Proceedings* - **MIRANDA, H. L. S.**; RABELO, CASSIANO; JORIO, ADO. Large Scale Automatic Data Analysis Tools for sp2 Carbon. 2017. (Oral and poster presentation, 18th International Conference on the Science and Application of Nanotubes and Low-dimensional Materials)

- *Software Copyright* - ADO JORIO ; CASSIANO RABELO ; **MIRANDA, HUDSON** ; CANÇADO, LUIZ GUSTAVO . Probe Master. 2020. Type: Computer

Program. Register number: BR512020001027-0, dated: 05/06/2020, titled: "Probe Master" , Institution of register: INPI - Instituto Nacional da Propriedade Industrial.

These works were also developed during this period in collaboration with other scientists, but regard other aspects of the TERS system and Raman spectroscopy, not being documented in this thesis:

- *Journal Paper* - FONSECA, EMERSON A. ; LAFETÁ, LUCAS ; CUNHA, RENAN ; **MIRANDA, HUDSON** ; CAMPOS, JOÃO ; MEDEIROS, HELTON G. ; ROMANO-SILVA, MARCO A. ; SILVA, RAIGNA A. ; BARBOSA, ALEXANDRE S. ; VIEIRA, RAFAEL P. ; MALARD, LEANDRO M. ; JORIO, ADO . A fingerprint of amyloid plaques in a bitransgenic animal model of Alzheimer's disease obtained by statistical unmixing analysis of hyperspectral Raman data. ANALYST, v. 144, p. 7049-7056, 2019.

- *Journal Paper* - ALENCAR, R. S. ; RABELO, CASSIANO ; **MIRANDA, HUDSON L. S.** ; VASCONCELOS, THIAGO L. ; OLIVEIRA, BRUNO S. ; RIBEIRO, AROLDO ; PÚBLIO, BRUNO C. ; RIBEIRO-SOARES, JENAINA ; FILHO, A. G. SOUZA ; CANÇADO, LUIZ GUSTAVO ; JORIO, ADO . Probing Spatial Phonon Correlation Length in Post-Transition Metal Monochalcogenide GaS Using Tip-Enhanced Raman Spectroscopy. NANO LETTERS, v. 19, p. 7357-7364, 2019.

- *Journal Paper* - SILVA, DIEGO L. ; CAMPOS, JOÃO LUIZ E. ; FERNANDES, THALES F.D. ; ROCHA, JERONIMO N. ; MACHADO, LUCAS R.P. ; SOARES, EDER M. ; MIQUITA, DOUGLAS R. ; **MIRANDA, HUDSON** ; RABELO, CASSIANO ; VILELA NETO, OMAR P. ; JORIO, ADO ; CANÇADO, LUIZ GUSTAVO . Raman spectroscopy analysis of number of layers in mass-produced graphene flakes. CARBON, v. 161, p. 181-189, 2020.

- *Journal Paper* - R. S. ALENCAR; R. LONGUINHOS; C. RABELO; **H. MIRANDA**; B. C. VIANA, A. G. SOUZA FILHO; L. G. CANCADO; A. JORIO; J. RIBEIRO-SOARES. Raman spectroscopy polarization dependence analysis in two-dimensional gallium sulfide. Phys. Rev. B, Accepted for publication.

- *Complete Work in Conference Proceedings* - AMORIM, LAURA; **MIRANDA, HUDSON**; MELO, JOHNATHAN; RABELO, CASSIANO; CANCADO, LUIZ GUSTAVO; ETRUSCO, LUIZ FERNANDO; JORIO, ADO. Vision-based position control applied to probe positioning for Tip Enhanced Raman Spectroscopy. In: 2016 1st International Symposium on Instrumentation Systems, Circuits and Transducers (INSCIT), 2016, Belo Horizonte. 2016 1st International Symposium on Instrumentation Systems, Circuits and Transducers (INSCIT), 2016. p. 81.

- *Complete Work in Conference Proceedings* - RABELO, CASSIANO ; **MIRANDA, HUDSON** ; VASCONCELOS, THIAGO L. ; CANCADO, LUIZ GUSTAVO ; JORIO, ADO . Tip-enhanced Raman Spectroscopy of Graphene. In: 2019 4th International Symposium on Instrumentation Systems, Circuits and Transducers (INSCIT), 2019, Sao Paulo. 2019 4th International Symposium on Instrumentation Systems, Circuits and Transducers (INSCIT), 2019. p. 1.

- *Complete Work in Conference Proceedings* - FREITAS, TIAGO ABREU ; **MIRANDA, HUDSON** ; RABELO, CASSIANO ; JORIO, ADO . Instrumentation and Algorithms for the Sonification of Scanning Probe Microscopy Output. In: 2018 3rd International Symposium on Instrumentation Systems, Circuits and Transducers (INSCIT), 2018, Bento Gonçalves. 2018 3rd International Symposium on Instrumentation Systems, Circuits and Transducers (INSCIT), 2018. p. 1.

- *Complete Work in Conference Proceedings* - TIAGO ABREU FREITAS ; **HUDSON MIRANDA** ; CASSIANO RABELO ; ADO JORIO . Implementação de sistema para sonificação de microscopia de varredura por sonda. In: XXII Congresso Brasileiro de Automática, 2018, João Pessoa, 2018.

- *Patent Application* - AMORIN, L. P. C.; **MIRANDA, H. L. S.**; MELO NETO, J. M.; JORIO, A.; CANCADO, L. G. O. L.; SILVA, C. R. E.; MENDES, L. T. S.; VASCONCELOS, T. L. E.; OLIVEIRA, B. S.; ARCHANJO, B. S.; ACHETE, C. A.; MOREIRA, L. F. E.. Método de Posicionamento Automático para Montagem de Sondas para Varredura e Espectroscopia Óptica In Situ e Dispositivo. 2017, Brasil. Patente: Privilégio de Inovação. Registry: BR1020170079171, Title: 'Método de Posicionamento Automático para Montagem de Sondas para Varredura e Espectroscopia Óptica In Situ e Dispositivo', Register Institution: INPI - Instituto Nacional da Propriedade Industrial, Applicant(s) : Universidade Federal de Minas Gerais;Instituto Nacional de Metrologia, Qualidade e Tecnologia, Deposit Date: 17/04/2017.

- *Patent Application* - ENGEL, M. ; STEINER, M. ; JORIO, ADO ; RABELO, CASSIANO ; CANCADO, LUIZ GUSTAVO ; **MIRANDA, HUDSON**. Calibrating tip-enhanced raman microscopes. 2018, Estados Unidos. Type: Innovation Privilege. Register number: US20190383854A1, titled: "Calibrating tip-enhanced raman microscopes" , Institution of register: United States Patent and Trademark Office. Dated: 17/06/2018.

- *Software Copyright* - ADO JORIO ; CASSIANO RABELO ; **MIRANDA, HUDSON** ; CANÇADO, LUIZ GUSTAVO . Focus Master. 2020. Type: Computer Program. Register number: BR512020001026-1, dated: 05/06/2020, titled: "Focus Master" , Institution of register: INPI - Instituto Nacional da Propriedade Industrial.

Bibliography

[1] E. Abbe. "VII.-On the Estimation of Aperture in the Microscope." In: *Journal of the Royal Microscopical Society* 1.3 (1881), pp. 388–423. ISSN: 03683974. DOI: 10.1111/j.1365-2818.1881.tb05909.x. URL: http://doi.wiley.com/10.1111/j.1365-2818.1881.tb05909.x.

[2] IBiology. *Microscopy: Resolution*. 2012. URL: https://www.ibiology.org/talks/resolution-of-a-microscope/ (visited on 01/10/2019).

[3] Lukas Novotny and Bert Hecht. *Principles of Nano-Optics*. Cambridge: Cambridge University Press, 2012. ISBN: 9780511794193. DOI: 10.1017/CBO9780511794193. URL: http://ebooks.cambridge.org/ref/id/CBO9780511794193.

[4] Michael Davidson. *Numerical Aperture and Image Resolution*. 2018. URL: https://www.microscopyu.com/tutorials/imageformation-airyna (visited on 06/08/2018).

[5] Stefan W Hell. "Nobel Lecture: Nanoscopy with freely propagating light". In: *Reviews of Modern Physics* 87.4 (2015), pp. 1169–1181. ISSN: 0034-6861. DOI: 10.1103/RevModPhys.87.1169. URL: https://link.aps.org/doi/10.1103/RevModPhys.87.1169.

[6] Takuya Tsuzuki. "Commercial scale production of inorganic nanoparticles". In: *International Journal of Nanotechnology* 6.5/6 (2009), p. 567. ISSN: 1475-7435. DOI: 10.1504/IJNT.2009.024647. URL: http://www.inderscience.com/link.php?id=24647.

[7] Feng Shao and Renato Zenobi. "Tip-enhanced Raman spectroscopy: principles, practice, and applications to nanospectroscopic imaging of 2D materials". In: *Analytical and Bioanalytical Chemistry* 411.1 (2019), pp. 37–61. ISSN: 1618-2642. DOI: 10.1007/s00216-018-1392-0. URL: http://link.springer.com/10.1007/s00216-018-1392-0.

[8] C. V. Raman. "A New Type of Secondary Radiation : Abstract : Nature". In: *Nature* 121 (1928), p. 501. ISSN: 0028-0836. DOI: 10.1038/121501c0. arXiv: arXiv:1011.1669v3. URL: http://www.nature.com/nature/journal/v121/n3048/abs/121501c0.html.

[9] Bert Voigtländer. *Scanning Probe Microscopy*. 2015, p. 375. ISBN: 978-3-662-45239-4. DOI: 10.1007/978-3-662-45240-0. arXiv: arXiv:1011.1669v3. URL: http://link.springer.com/10.1007/978-3-662-45240-0.

[10] Paulo Trindade. "Study of the Electrostatic Shielding and Environmental Interactions in Carbon Nanotubes by Resonance Raman". PhD thesis. Universidade Federal de Minas Gerais, 2010, pp. 42–105.

[11] Derek Nowak. "The Design of a Novel Tip Enhanced Near-field Scanning Probe Microscope for Ultra-High Resolution Optical Imaging". 2010.

[12] D.A. Schmidt, I. Kopf, and E. Bründermann. "A matter of scale: from far-field microscopy to near-field nanoscopy". In: *Laser & Photonics Reviews* 6.3 (2012), pp. 296–332. ISSN: 18638880. DOI: 10.1002/lpor.201000037. URL: http://linkinghub.elsevier.com/retrieve/pii/S0304399197000776http://doi.wiley.com/10.1002/lpor.201000037.

[13] Ado Jorio et al. *Raman Spectroscopy in Graphene Related Systems*. Weinheim, Germany: Wiley-VCH Verlag GmbH & Co. KGaA, 2011. ISBN: 9783527632695. DOI: 10.1002/9783527632695. URL: http://doi.wiley.com/10.1002/9783527632695.

[14] A. C. Ferrari et al. "Raman spectrum of graphene and graphene layers". In: *Physical Review Letters* 97.18 (2006), pp. 1–4. ISSN: 00319007. DOI: 10.1103/PhysRevLett.97.187401. arXiv: 0606284v1 [cond-mat].

[15] Ado Jorio. "Raman Spectroscopy in Graphene-Based Systems: Prototypes for Nanoscience and Nanometrology". In: *ISRN Nanotechnology* 2012.2 (2012), pp. 1–16. DOI: 10.5402/2012/234216.

[16] Harald Budde et al. "Raman Radiation Patterns of Graphene". In: *ACS Nano* 10.2 (2016), pp. 1756–1763. ISSN: 1936086X. DOI: 10.1021/acsnano.5b06631.

[17] Dara Bayat et al. "Dynamic behavior of the tuning fork AFM probe". In: *Microelectronic Engineering* 85.5-6 (2008), pp. 1018–1021. ISSN: 01679317. DOI: 10.1016/j.mee.2008.01.100.

[18] Hudson Miranda et al. "Study of the interaction between light and nanoantennas in Tip-Enhanced Raman Spectroscopy". In: *2019 4th International Symposium on Instrumentation Systems, Circuits and Transducers (INSCIT)*. IEEE, 2019, pp. 1–5. ISBN: 978-1-7281-2109-3. DOI: 10.1109/INSCIT.2019.8868513. URL: https://ieeexplore.ieee.org/document/8868513/.

[19] Lukas Novotny, Erik J. Sánchez, and X. Sunney Xie. "Near-field optical imaging using metal tips illuminated by higher-order Hermite-Gaussian beams". In: *Ultramicroscopy* 71.1-4 (1998), pp. 21–29. ISSN: 03043991. DOI: 10.1016/S0304-3991(97)00077-6.

[20] Thiago L. Vasconcelos et al. "Plasmon-Tunable Tip Pyramids: Monopole Nanoantennas for Near-Field Scanning Optical Microscopy". In: *Advanced Optical Materials* 6.20 (2018), p. 1800528. ISSN: 21951071. DOI: 10.1002/adom.201800528. URL: http://doi.wiley.com/10.1002/adom.201800528.

[21] Cassiano Rabelo et al. "Linkage Between Micro- and Nano-Raman Spectroscopy of Defects in Graphene". In: *Physical Review Applied* 14.2 (2020), p. 024056. ISSN: 2331-7019. DOI: 10.1103/PhysRevApplied.14.024056. URL: https://doi.org/10.1103/PhysRevApplied.14.024056https://link.aps.org/doi/10.1103/PhysRevApplied.14.024056.

[22] Rodolfo V. Maximiano et al. "Mechanism of near-field Raman enhancement in two-dimensional systems". In: *Physical Review B* 85.23 (2012), p. 235434. ISSN: 1098-0121. DOI: 10.1103/PhysRevB.85.235434. URL: https://link.aps.org/doi/10.1103/PhysRevB.85.235434.

[23] Thiago L Vasconcelos et al. "Optical Nanoantennas for Tip-Enhanced Raman Spectroscopy". In: *IEEE Journal of Selected Topics in Quantum Electronics* c (2020), pp. 1–1. ISSN: 1077-260X. DOI: 10.1109/JSTQE.2020.3008526. URL: https://ieeexplore.ieee.org/document/9138720/.

[24] Lucas C P A M Mu et al. "Strain Discontinuity, Avalanche, and Memory in Carbon Nanotube Serpentine Systems". In: (2015). DOI: 10.1021/acs.nanolett.5b01982.

[25] Ado Jorio and Luiz Gustavo Cançado. "Perspectives on Raman spectroscopy of graphene-based systems: From the perfect two-dimensional surface to charcoal". In: *Physical Chemistry Chemical Physics* 14.44 (2012), pp. 15246–15256. ISSN: 14639076. DOI: 10.1039/c2cp42621h.

[26] M.S. Dresselhaus, A. Jorio, and R. Saito. "Characterizing Graphene, Graphite, and Carbon Nanotubes by Raman Spectroscopy". In: *Annual Review of Condensed Matter Physics* 1.1 (2010), pp. 89–108. ISSN: 1947-5454. DOI: 10.1146/annurev-conmatphys-070909-103919. URL: http://www.annualreviews.org/doi/10.1146/annurev-conmatphys-070909-103919.

[27] Ryan Beams. "Tip-enhanced Raman scattering of graphene". In: *Journal of Raman Spectroscopy* 49.1 (2018), pp. 157–167. ISSN: 10974555. DOI: 10.1002/jrs.5211.

[28] Jan Rogalski et al. "STM tip-enhanced Raman spectroscopy and the investigation of doped graphene". In: *Vibrational Spectroscopy* 91 (2017), pp. 128–135. ISSN: 09242031. DOI: 10.1016/j.vibspec.2016.09.023. URL: http://dx.doi.org/10.1016/j.vibspec.2016.09.023.

[29] Melissa Paulite et al. "Full Spectroscopic Tip-Enhanced Raman Imaging of Single Nanotapes Formed from β-Amyloid(1–40) Peptide Fragments". In: *ACS Nano* 7.2 (2013), pp. 911–920. ISSN: 1936-0851. DOI: 10.1021/nn305677k. URL: http://pubs.acs.org/doi/10.1021/nn305677k.

[30] Alistair P D Elfick, Andrew R. Downes, and Rabah Mouras. "Development of tip-enhanced optical spectroscopy for biological applications: A review". In: *Analytical and Bioanalytical Chemistry* 396.1 (2010), pp. 45–52. ISSN: 16182642. DOI: 10.1007/s00216-009-3223-9.

[31] R Zhang et al. "Chemical mapping of a single molecule by plasmon-enhanced Raman scattering." In: *Nature* 498.7452 (2013), pp. 82–6. ISSN: 1476-4687. DOI: 10.1038/nature12151. URL: http://www.ncbi.nlm.nih.gov/pubmed/23739426.

[32] Jian-Ming Jin. *Theory and Computation of Electromagnetic Fields*. Ed. by Wiley-Blackwell. Hoboken, NJ, USA: John Wiley & Sons, Inc., 2010. ISBN: 9780470874257. DOI: 10.1002/9780470874257. arXiv: arXiv:1011.1669v3. URL: https://books.google.com/books?id=NDV0CgAAQBAJ{\&}pgis=1https://www.cambridge.org/core/product/identifier/CBO9781107415324A009/type/book{_}parthttp://doi.wiley.com/10.1002/9780470874257.

[33] P. B. Johnson and R. W. Christy. "Optical Constants of the Noble Metals". In: *Physical Review B* 6.12 (1972), pp. 4370–4379. ISSN: 0556-2805. DOI: 10.1103/PhysRevB.6.4370. arXiv: arXiv:1011.1669v3. URL: https://link.aps.org/doi/10.1103/PhysRevB.6.4370.

[34] R. Mittra et al. "A review of absorbing boundary conditions for two and three-dimensional electromagnetic scattering problems". In: *IEEE Transactions on Magnetics* 25.4 (1989), pp. 3034–3039. ISSN: 00189464. DOI: 10.1109/20.34361. URL: http://ieeexplore.ieee.org/document/34361/.

[35] Z.S. Sacks et al. "A perfectly matched anisotropic absorber for use as an absorbing boundary condition". In: *IEEE Transactions on Antennas and Propagation* 43.12 (1995), pp. 1460–1463. ISSN: 0018926X. DOI: 10.1109/8.477075. URL: http://ieeexplore.ieee.org/document/477075/.

[36] João Luiz Elias Campos et al. "Applications of Raman spectroscopy in graphene-related materials and the development of parameterized PCA for large-scale data analysis". In: *Journal of Raman Spectroscopy* 49.1 (2018), pp. 54–65. ISSN: 03770486. DOI: 10.1002/jrs.5225. URL: http://doi.wiley.com/10.1002/jrs.5225.

[37] Holly J Butler et al. "Using Raman spectroscopy to characterise biological materials". In: *Nature Protocols* 11.4 (2016), pp. 1–47. ISSN: 1754-2189. DOI: 10.1038/nprot.2016.036. URL: http://dx.doi.org/10.1038/nprot.2016.036.

[38] Diego L. Silva et al. "Raman spectroscopy analysis of number of layers in mass-produced graphene flakes". In: *Carbon* 161 (2020), pp. 181–189. ISSN: 00086223. DOI: 10.1016/j.carbon.2020.01.050. URL: https://linkinghub.elsevier.com/retrieve/pii/S0008622320300567.

[39] Chein-I Chang. *Hyperspectral Data Processing*. Hoboken, NJ, USA: John Wiley & Sons, Inc., 2013. ISBN: 9781118269787. DOI: 10.1002/9781118269787. URL: http://doi.wiley.com/10.1002/9781118269787.

[40] Song Jiang et al. "Subnanometer-resolved chemical imaging via multivariate analysis of tip-enhanced Raman maps". In: *Light: Science & Applications* 6.11 (2017), e17098. ISSN: 2047-7538. DOI: 10.1038/lsa.2017.98. URL: http://www.nature.com/doifinder/10.1038/lsa.2017.98.

[41] Tanja Deckert-Gaudig et al. "Spatially resolved spectroscopic differentiation of hydrophilic and hydrophobic domains on individual insulin amyloid fibrils". In: *Scientific Reports* 6.1 (2016), p. 33575. ISSN: 2045-2322. DOI: 10.1038/srep33575. URL: http://dx.doi.org/10.1038/srep33575http://www.nature.com/articles/srep33575.

[42] Emerson A. Fonseca et al. "A fingerprint of amyloid plaques in a bitransgenic animal model of Alzheimer's disease obtained by statistical unmixing analysis of hyperspectral Raman data". In: *Analyst* 144.23 (2019), pp. 7049–7056. ISSN: 13645528. DOI: 10.1039/c9an01631g. URL: http://xlink.rsc.org/?DOI=C9AN01631G.

[43] Gareth James et al. *An Introduction to Statistical Learning*. Vol. 103. Springer Texts in Statistics. New York, NY: Springer New York, 2013, p. 618. ISBN: 978-1-4614-7137-0. DOI: 10.1007/978-1-4614-7138-7. arXiv: arXiv:1011.1669v3. URL: http://books.google.com/books?id=9tv0taI8l6YChttp://link.springer.com/10.1007/978-1-4614-7138-7.

[44] Chein I. Chang, Chao Cheng Wu, and Ching Tsorng Tsai. "Random N-finder (N-FINDR) endmember extraction algorithms for hyperspectral imagery". In: *IEEE Transactions on Image Processing* 20.3 (2011), pp. 641–656. ISSN: 10577149. DOI: 10.1109/TIP.2010.2071310.

[45] D.C. Heinz and Chein-I-Chang. "Fully constrained least squares linear spectral mixture analysis method for material quantification in hyperspectral imagery". In: *IEEE Transactions on Geoscience and Remote Sensing* 39.3 (2001), pp. 529–545. ISSN: 01962892. DOI: 10.1109/36.911111. URL: http://ieeexplore.ieee.org/document/774644/http://ieeexplore.ieee.org/document/911111/.

[46] Marc Richter et al. "Laterally resolved and direct spectroscopic evidence of nanometer-sized lipid and protein domains on a single cell". In: *Small* 7.2 (2011), pp. 209–214. ISSN: 16136810. DOI: 10.1002/smll.201001503.

[47] Gilad M. Lerman and Uriel Levy. "Effect of radial polarization and apodization on spot size under tight focusing conditions". In: *Optics Express* 16.7 (2008), p. 4567. ISSN: 1094-4087. DOI: 10.1364/OE.16.004567. URL: https://www.osapublishing.org/oe/abstract.cfm?uri=oe-16-7-4567.

[48] Max Berek. "Pioneers in Optics: Max Berek". In: *Microscopy Today* 24.5 (2016), pp. 44–45. ISSN: 1551-9295. DOI: 10.1017/S1551929516000717. URL: https://www.cambridge.org/core/product/identifier/S1551929516000717/type/journal{_}article.

[49] Thiago L. Vasconcelos et al. *Dispositivo Metálico para Microscopia por Varredura por Sonda e Método de Fabricação do Mesmo*. 2015. URL: https://patents.google.com/patent/WO2017103789A1.

[50] Thiago L. Vasconcelos et al. "Tuning Localized Surface Plasmon Resonance in Scanning Near-Field Optical Microscopy Probes". In: *ACS Nano* 9.6 (2015), pp. 6297–6304. ISSN: 1936-0851. DOI: 10.1021/acsnano.5b01794. URL: https://pubs.acs.org/doi/10.1021/acsnano.5b01794.

[51] Martin Nawrath. *Arduino Frequency Counter Library*. 2012. URL: http://interface.khm.de/index.php/lab/interfaces-advanced/arduino-frequency-counter-library/ (visited on 07/18/2018).

[52] B Y Antoine Ferreira and Constantinos Mavroidis. "Virtual Reality and Haptics for Nanorobotics". In: *Image (Rochester, N.Y.)* September (2006).

[53] Morgan Quigley et al. "ROS: an open-source Robot Operating System". In: *Icra* 3 (2009), p. 5. ISSN: 0165-022X. DOI: http://www.willowgarage.com/papers/ros-open-source-robot-operating-system. arXiv: 1106.4561. URL: http://pub1.willowgarage.com/{~}konolige/cs225B/docs/quigley-icra2009-ros.pdf.

[54] Brandon Itkowitz, Josh Handley, and Weihang Zhu. "The OpenHaptics™ toolkit: A library for adding 3D Touch™ navigation and haptics to graphics applications". In: *Proceedings - 1st Joint Eurohaptics Conference and Symposium on Haptic Interfaces for Virtual Environment and Teleoperator Systems; World Haptics Conference, WHC 2005* (2005), pp. 590–591. DOI: 10.1109/WHC.2005.133.

[55] Christian Therien. *PySptools*. 2018. URL: https://pysptools.sourceforge.io/index.html (visited on 02/05/2018).

[56] Hudson Miranda et al. "Impact of substrate on tip-enhanced Raman spectroscopy: A comparison between field-distribution simulations and graphene measurements". In: *Physical Review Research* 2.2 (2020), p. 023408. ISSN: 2643-1564. DOI: 10.1103/PhysRevResearch.2.023408. arXiv: 2001.06688. URL: http://arxiv.org/abs/2001.06688https://link.aps.org/doi/10.1103/PhysRevResearch.2.023408.

[57] Hudson Miranda et al. "Optical Properties of Plasmon-Tunable Tip Pyramids for Tip-Enhanced Raman Spectroscopy". In: *physica status solidi (RRL) – Rapid Research Letters* 2000212 (2020), p. 2000212. ISSN: 1862-6254. DOI: 10.1002/pssr.202000212. URL: https://onlinelibrary.wiley.com/doi/abs/10.1002/pssr.202000212.

[58] Jeffrey M. McMahon, Stephen K. Gray, and George C. Schatz. "Calculating nonlocal optical properties of structures with arbitrary shape". In: *Physical Review B* 82.3 (2010), p. 035423. ISSN: 1098-0121. DOI: 10.1103/PhysRevB.82.035423. URL: https://link.aps.org/doi/10.1103/PhysRevB.82.035423.

[59] Challa S.S.R. Kumar. *Raman Spectroscopy for Nanomaterials Characterization*. Ed. by Challa S. S. R. Kumar. Vol. 9783642206. Berlin, Heidelberg: Springer Berlin Heidelberg, 2012, pp. 1–645. ISBN: 978-3-642-20619-1. DOI: 10.1007/978-3-642-20620-7. URL: http://materials.springer.com/bp/docs/978-3-642-20620-7.

[60] Simon F. Becker et al. "Gap-Plasmon-Enhanced Nanofocusing Near-Field Microscopy". In: *ACS Photonics* 3.2 (2016), pp. 223–232. ISSN: 23304022. DOI: 10.1021/acsphotonics.5b00438.

[61] Judith Langer et al. "Present and Future of Surface-Enhanced Raman Scattering". In: *ACS Nano* 14.1 (2020), pp. 28–117. ISSN: 1936-0851. DOI: 10.1021/acsnano.9b04224. URL: https://pubs.acs.org/doi/10.1021/acsnano.9b04224.

[62] Florian Schulz, Steffen Tober, and Holger Lange. "Size-Dependent Phase Transfer Functionalization of Gold Nanoparticles To Promote Well-Ordered Self-Assembly". In: *Langmuir* 33.50 (2017), pp. 14437–14444. ISSN: 0743-7463. DOI: 10.1021/acs.langmuir.7b03600. URL: https://pubs.acs.org/doi/10.1021/acs.langmuir.7b03600.

[63] Zhilin Yang, Javier Aizpurua, and Hongxing Xu. "Electromagnetic field enhancement in TERS configurations". In: *Journal of Raman Spectroscopy* 40.10 (2009), pp. 1343–1348. ISSN: 03770486. DOI: 10.1002/jrs.2429.